

Simple tools to study global dynamics in non-axisymmetric galactic potentials – I

P.M. Cincotta^{1,*} and C. Simó^{2,**}

¹ Facultad de Ciencias Astronómicas y Geofísicas, Universidad Nacional de La Plata, Paseo del Bosque, 1900 La Plata, Argentina

² Departament de Matemàtica Aplicada i Anàlisi, Universitat de Barcelona, Gran Via 585, 08007 Barcelona, Spain

Received July 30, 1999; accepted September 4, 2000

Abstract. In a first part we discuss the well-known problem of the motion of a star in a general non-axisymmetric 2D galactic potential by means of a very simple but almost universal system: the pendulum model. It is shown that both loop and box families of orbits arise as a natural consequence of the dynamics of the pendulum. An approximate invariant of motion is derived. A critical value of the latter sharply separates the domains of loops and boxes and a very simple computation allows to get a clear picture of the distribution of orbits on a given energy surface. Besides, a geometrical representation of the global phase space using the natural surface of section for the problem, the 2D sphere, is presented. This provides a better visualization of the dynamics.

In a second part we introduce a new indicator of the basic dynamics, the Mean Exponential Growth factor of Nearby Orbits (MEGNO), that is suitable to investigate the phase space structure associated to a general Hamiltonian. When applied to the 2D logarithmic potential it is shown to be effective to obtain a picture of the global dynamics and, also, to derive good estimates of the largest Lyapunov characteristic number in realistic physical times. Comparisons with other techniques reveal that the MEGNO provides more information about the dynamics in the phase space than other wide used tools.

Finally, we discuss the structure of the phase space associated to the 2D logarithmic potential for several values of the semiaxis ratio and energy. We focus our attention on the stability analysis of the principal periodic orbits and on the chaotic component. We obtain critical energy values for which connections between the main stochastic zones take place. In any case, the whole chaotic domain appears to be always confined to narrow filaments, with a Lyapunov time about three characteristic periods.

Key words: galaxies: dynamics — stellar dynamics — methods: analytical-numerical — chaos

1. Introduction

Galaxies behave as collisionless systems. If $\mathcal{N} \gg 1$ is the number of stars in a galaxy, the collisionless condition allows to reduce the full \mathcal{N} -particle probability density to the single-particle density, $f(\mathbf{x}, t)$, where \mathbf{x} is the phase space vector of any star. The density f obeys the collisionless Boltzmann equation in which the interaction term is reduced to a smooth potential, $\nabla^2\phi(\mathbf{q}; t) \equiv 4\pi G\mathcal{N} \int f(\mathbf{q}, \mathbf{p}; t)d^3p$, generated by the whole galaxy.

Of most importance are steady state solutions of Boltzmann's equation. To find out these solutions we need a priori some knowledge about the orbital structure supported by the static potential $\phi(\mathbf{q})$. As the strong Jeans theorem states, f should depend on the phase space variables only through the integrals of motion, I_1, I_2, I_3 , associated to $\phi(\mathbf{q})$ (see Binney & Tremaine 1987, BT87 hereafter). The theorem makes sense when the field is integrable, that is, when the motion is completely regular (and quasiperiodic). In general this is not the case for realistic galactic potentials. If irregular motion occupies a comparatively large fraction of phase space then a different interpretation of the strong Jeans theorem is needed (see, for example, Merritt & Valluri 1996).

In the present work we consider a given potential $\phi(\mathbf{r})$, being the orbits in this field the building blocks of a galaxy. This is a rough approximation to, say, an elliptical galaxy since we are neglecting the presence of gas, tidal effects, rotation, the irregularities of the potential due to the irregular dynamics, etc. Within all possible choices of $\phi(\mathbf{r})$, one should take realistic models. This was done for instance by Merritt & Friedman (1996), Merritt & Valluri (1996), where they take a Dehnen's (1993) law for the density

Send offprint requests to: P.M. Cincotta

* e-mail: pmc@fcaglp.unlp.edu.ar

** e-mail: carles@maia.ub.es

that, in turn, leads to a triaxial potential. Thus ϕ is expected to be a complicated function of the position or, as in the latter case, no analytical expression can be obtained for it. In this direction, to perform numerical investigations it is convenient, in a first systematic study, to simplify even more the problem by assuming the potential given by a simple and well-behaved function of the position. This will be our present approach.

Having the potential the efforts are devoted to obtain a picture of the global dynamics. That is, for any energy level to look for families of orbits related to the main periodic orbits and also to identify stochastic components. This is suitable for 2D systems because resonant tori mean periodic orbits but for 3D systems resonant tori mean, in general, 2D tori. For the stochastic regions it is relevant to have estimates of the time-scale for the manifestation of chaos in the orbital motion, the so-called Lyapunov time defined as the inverse of the largest Lyapunov characteristic number (LCN hereafter – see, for example, Reichl 1992). Stochastic components for which the Lyapunov time is much larger than the Hubble time can be regarded as regular for practical purposes.

To cope with the whole problem one could apply analytical tools developed for the study of Hamiltonian systems. But several questions restrict this approach. As an example let us mention that almost all the useful theorems deal with a special kind of systems, the so-called near-integrable Hamiltonian systems, and can be written in terms of action-angle variables. Its main part only depends on the actions, while the remainder that depends on both actions and angles, is considered as a small perturbation. This approximation is largely used for some problems in Celestial Mechanics but in Galactic Dynamics it seems that is not possible, in general, to perform the separation between an unperturbed Hamiltonian and a perturbation. Therefore this nice set of variables appears to be unsuitable to study, globally, the dynamics of galaxies. Yet, some attempts to compute such variables can be found in the literature (see for example McGill & Binney 1990; Binney & Spergel 1984; Papaphilippou & Laskar 1996 – PL96 hereafter). Hence in almost all cases the study should be done by means of numerical tools and the obtained results rest mainly in those numerical experiments rather than in rigorous theorems.

From the above discussion it turns out that it would be useful to have at hand a simple procedure to derive the basic dynamics. The phase space associated to a realistic Hamiltonian contains ordered and chaotic components. No additional global integrals besides the energy exist. However, if chaotic motion is confined to a comparatively small region of the phase space, regular motion should respect some other (perhaps local) “pseudo-invariants” and then it is in principle possible to obtain a picture of the dynamics. In fact, this remark is what justifies the attempts to compute (numerically) the actions in certain galactic potentials. This was also the spirit

behind the search for the so-called third integral of motion, the Hénon & Heiles (1964) famous paper being a pioneer work in this sense. Generically a “third integral” (or convergent normal form or adelic integral using an old fashioned name due to Whittaker 1917) does not exist but, for some ranges of the energy (or any other parameter), formal expansions can be useful as quasi-invariants to have a good description of the phase space. Different approaches to construct equilibrium models of galaxies were done by means of fully integrable potentials, like that of Stäckel form (see, for instance, Dejonghe & de Zeeuw 1988; de Zeeuw & Pfenniger 1988) or using models that allow for an approximate third integral (Petrou 1983a,b – see Sect. 2.1).

In recent years, however, the discussion is focused on the relevance of chaotic motion in models of elliptical galaxies. There is numerical evidence that, for instance, triaxial systems with a central strong cusp (simulating a mass concentration or black hole) contain a large amount of chaos (see Merritt & Valluri 1996; Valluri & Merritt 1998). A wide-spread tool used to identify regular and chaotic orbits and to estimate the time-scale over which chaos is relevant, is the computation of the LCN (or the KS entropy) for a set of orbits over motion times which are $\lesssim 10^4$ periods. Motion times about 10^4 periods are lower bounds to reach a good estimate of the LCN. Indeed $\sim 10^5 - 10^6$ periods are necessary to obtain an accurate determination (see Sect. 4). For the sake of comparison and to keep in mind a realistic time scale, we recall that the Hubble time is in the order of $10^2, 10^3$ periods as much. In any case, motion times $\gtrsim 10^4$ periods turn out to be too large (in a computational sense) when we deal with 10^5 or 10^6 orbits. The situation is even worst if the potential has not a simple analytical expression, the computing time being quite long in this case. For instance, Merritt & Valluri (1996) reported that, for their model, the time needed to integrate a single orbit and its variationals over 10^4 periods to get the two positive Lyapunov exponents was about 80 minutes in a DEC Alpha 3000/700 workstation¹.

Alternative techniques were proposed to separate ordered and stochastic motion, to classify orbits in families, to describe the global structure of phase space, but not to get the LCN in shorter times. In Sect. 6 we shall resume this point together with some comparisons with the new technique here presented (MEGNO).

In Sect. 2 we discuss a simple, heuristic but effective, way to understand the different types of orbits in general 2D non-axisymmetric galactic potentials. Even though some qualitative ideas behind this approach were sketched, for instance, by Binney & Spergel (1982), Contopoulos & Seimenis (1990), Cincotta (1993),

¹ An array of processors in parallel makes possible to cope with large sets of orbits to perform, e.g., a fine scanning of the parameter space of a given Hamiltonian.

Cincotta et al. (1996), in this work we take advantage of the pendulum model to show that the main families of orbits, loop and box, respect, besides the energy, *the same* approximate invariant of motion. This approximation rests on the so-called ideal resonance problem largely discussed in the past (see for example Garfinkel 1966). The explicit derivation of this rough third integral leads to illustrative pictures of the orbital distribution at a given energy level being then, in principle, unnecessary the numerical calculation of the action integrals.

In Sect. 3 we sketch a representation of the global phase space useful to display the full dynamics, for a given energy level, on a single picture. It rests on the computation of a standard surface of section but instead of using a 2D plane we consider the natural manifold for the problem, which in this case corresponds to the 2D sphere.

In Sect. 4 we introduce the Mean Exponential Growth factor of Nearby Orbits (MEGNO). This new tool has proven to be useful for studying global dynamics and succeeds in revealing the hyperbolic structure of phase-space, the source of chaotic motion. The MEGNO provides a measure of chaos that is proportional to the LCN, so that it allows to derive the actual LCN but in realistic physical times, $\sim 10^3$ periods. At least for the example discussed here, the MEGNO seems to provide more information about the dynamics than any other technique used before in this kind of applications.

As an example of non-axisymmetric galactic potential we study the 2D logarithmic model. We choose this potential to perform the numerical study because of three different reasons: i) a field with a simple analytic expression is easier to deal with; ii) it is, perhaps, a rough realistic model for the field acting on a star moving on the equatorial plane of a barlike galaxy or in the meridian plane of a spatial axisymmetric non-rotating elliptical galaxy; iii) it was largely studied, among others, by Binney & Spergel (1982, 1984), BT87, Miralda-Escudé & Schwarzschild (1989) – MS89 hereafter –, Lees & Schwarzschild (1992) and particularly by PL96 by means of the frequency map analysis. Therefore it allows to compare their results with the ones obtained here.

Finally, in Sect. 5, a survey is made of the most relevant features of the global dynamics for significant values of the energy and flatness of the potential.

A future paper will be devoted to the study of full 3D potentials by means of these or other simple tools.

2. Orbits in non-axisymmetric 2D potentials

2.1. Third integral and the pendulum model

In any 2D non-axisymmetric potential the main families of orbits are the so-called loop and box (BT87). Which family dominates the orbital structure depends mainly on the relative value of the rotational kinetic energy with

respect to the degree of flatness of the potential (see below). To describe the problem in a more general context, let us consider a spatial axisymmetric galaxy, where we assume that the potential depends on the position through $m_q(R, z) = R^2 + z^2/q^2$, (R, φ, z) being cylindrical coordinates and $q < 1$ the semiaxis ratio of isopotential curves in the Rz -plane. The potential is then $\phi(\mathbf{r}) = \Phi(m_q(R, z))$ where Φ is a smooth function of its argument.

In any case, 3D motion reduces to 2D motion in Cartesian coordinates if we introduce the effective potential $\Phi(m_q(R, z)) + p_\varphi^2/2R^2$, where p_φ is a global integral. As the second term is the same for any Φ , we focus the attention on the motion of a star in the 2D potential $\phi(x, y) = \Phi(m_q(x, y))$ where x, y are coordinates in some meridian plane by setting $p_\varphi = 0^2$. Alternatively, $\phi(x, y)$ could represent the motion in the equatorial plane ($z = 0$) of a barlike galaxy, being then x, y coordinates in the latter plane.

The equations of motion, in these variables, are

$$\dot{p}_x = -2\Phi'x, \quad \dot{p}_y = -2\Phi'y/q^2,$$

where $p_x = \dot{x}$, $p_y = \dot{y}$ and $\Phi' \equiv d\Phi/dm_q$ is assumed analytic everywhere. To be $-\nabla\phi$ a well defined gravitational field it is necessary to impose the conditions $\Phi' > 0$ and $\Phi'' < 0$. To understand the differences between both families of orbits one can follow different approaches. The “rigorous” one as follows. For box orbits, one should restrict the flow to the invariant planes $p_x = x = 0$ or $p_y = y = 0$ and to investigate the 1D Hamiltonians H_y and H_x , respectively. Take one of them and consider the other as a small perturbation. The next step is to analyse the stability of the periodic orbits in the unperturbed 1D Hamiltonians, at a given energy level, by a linearization of the equations of motion of the full Hamiltonian around these orbits (for instance by a Floquet analysis, see BT87 and Sect. 5). Similar considerations apply to loop orbits: just take values of q very close to 1 so that the field is nearly spherical and can be written as a near integrable one. The stability of the 1:1 (circular) periodic orbit is then analysed. This procedure is followed, for example, by MS89 and PL96 for the 2D logarithmic potential to conclude that, for the energies and values of q they studied, the short-axis periodic orbit (y -axis) is, in general, unstable while the long-axis orbit (x -axis) is, in general, stable for low-to-moderate energies (see Sect. 5). The 1:1 periodic orbit (that bifurcates from the y -axis orbit) turns out to be always stable for any physical value of q . Therefore, box orbits can be thought as perturbations to the x -axis periodic orbits while loop orbits arise from perturbations to the 1:1 (circular) periodic orbit in the spherical system.

² A value $p_\varphi \neq 0$ could change the topology of the phase space. The discussion given here could be slightly different, but the tools to study it are the same presented here. The main difference, if $p_\varphi \neq 0$, is that $R = 0$ is not admissible and box orbits do not exist.

A “physical” interpretation is the following. The angular momentum (or the rotational kinetic energy) plays a crucial role in the existence of both families of orbits. Indeed, take polar coordinates in the xy -plane: $x = r \cos \theta$, $y = r \sin \theta$, so $m_q \rightarrow m_\alpha = r^2(1 + \alpha \sin^2 \theta)$, where $\alpha = (1 - q^2)/q^2$. Due to the lack of central symmetry, a test star will be acted by a torque $N = -\partial\phi/\partial\theta = -\Phi' \partial m_\alpha / \partial \theta = -\alpha r^2 \Phi' \sin 2\theta$. If $\Phi' \neq 0$ then for any $r > 0$ the torque is null at $\theta = 0, \pi/2$ (and $\pi, -\pi/2$), that is, on the x and y axis. Recalling that $\dot{p}_\theta = N$, where p_θ is the angular momentum of the star, we conclude that an orbit with $p_\theta = 0$ will follow a rectilinear orbit along the x or y axis. A simple inspection of the expression for N shows that the torque is negative in the first and third quadrant, being positive in the others. Therefore, we see why the x -axis periodic orbit is stable while the y -axis one is unstable. The torque confines near the x -axis and pulls away near the y -axis. On the other hand, a simple epicycle approximation (see BT87, Lees & Schwarzschild 1992) shows that the 1:1 (circular) periodic orbit is naturally stable for α not too large.

Let us recall that this description is true provided that Φ is a smooth function of m_α . If the potential has a singularity or a cusp at the origin, then the analysis may be different. Therefore the discussion given above is suitable for potentials that are not “hard” at the origin, that is, those for which the deflection angle $\Delta\theta$ is close to π when $p_\theta \rightarrow 0$ (see BT87, MS89 for details).

Let us write the full Hamiltonian in polar coordinates

$$H(p_r, p_\theta, r, \theta) = \frac{p_r^2}{2} + \frac{p_\theta^2}{2r^2} + \Phi(m_\alpha(r, \theta)),$$

where $p_r = \dot{r}$, $p_\theta = r^2 \dot{\theta}$. Assume that α is small, that is, $1/\sqrt{2} < q \lesssim 1$, so we can expand $\Phi(m_\alpha(r, \theta))$ in powers of α and we can separate the part independent of θ

$$H(p_r, p_\theta, r, \theta) = p_r^2/2 + p_\theta^2/2r^2 + \phi_\alpha(r) - \frac{\alpha}{2} f_1(r) \cos 2\theta - \frac{\alpha^2}{4} f_2(r) (\cos 2\theta - \frac{1}{4} \cos 4\theta) + \dots, \quad (1)$$

where

$$\begin{aligned} \phi_\alpha(r) &= \Phi(r^2) + \frac{\alpha}{2} f_1(r) + \frac{3\alpha^2}{16} f_2(r) + \dots, \\ f_1(r) &= \Phi'(r^2) r^2 \geq 0, \quad f_2(r) = \Phi''(r^2) r^4 \leq 0. \end{aligned} \quad (2)$$

From (1) and (2) the Hamiltonian can be written as

$$H(p_r, p_\theta, r, \theta) = H_0(p_r, p_\theta, r) + \alpha V_1 + \alpha^2 V_2 + \dots,$$

$$H_0(p_r, p_\theta, r) = \frac{p_r^2}{2} + \frac{p_\theta^2}{2r^2} + \phi_\alpha(r), \quad (3)$$

$$V_n(r, \theta) = f_n(r) \sum_{m=1}^n a_m \cos 2m\theta, \quad f_n(r) = \Phi^{(n)}(r^2) r^{2n}.$$

H_0 is an integrable Hamiltonian being $H_0 = h_0$ itself and $p_\theta = p_\theta^0$ the unperturbed integrals and $\alpha^n V_n$ are small perturbations (see the remark at the end of this subsection). So, from now on, when we refer to unperturbed motion, we mean orbits in H_0 even though it depends on α .

The unperturbed system is just a central field. So r oscillates between two boundaries, $r_m(h_0, p_\theta^0) \leq r^o(t) \leq r_M(h_0, p_\theta^0)$, with frequency ω_r , while θ^o varies on the circle

\mathbb{S}^1 . The frequency in the tangential direction is $\omega_\theta = \kappa \omega_r$ where $\kappa = \Delta\theta/2\pi < 1$ is, in general, irrational. The time evolution of θ can be written as $\theta^o(t) = \omega_\theta t + \Theta(t)$ where Θ is a $2\pi/\omega_r$ -periodic function of time.

Let us focus the attention, in the perturbed system, on the dynamics in the tangential direction. Keeping terms up to first order in α in (3) we get

$$\dot{p}_\theta = -\frac{\partial H}{\partial \theta} \approx -\alpha \frac{\partial V_1}{\partial \theta} = -\alpha f_1(r) \sin 2\theta. \quad (4)$$

From (4) a simple manipulation shows that the latter can be written as

$$\frac{d\mathcal{K}}{dt} + \alpha g_1(r(t)) \sin 2\theta(t) \approx 0, \quad \mathcal{K} \equiv \frac{p_\theta^2}{2} - \frac{\alpha}{2} g \cos 2\theta, \quad (5)$$

where g and $g_1(r(t))$ are the average and oscillating parts of $f_1(r(t))r^2(t)$ respectively:

$$\begin{aligned} g &= \langle f_1(r)r^2 \rangle = \langle \Phi'(r^2)r^4 \rangle > 0, \\ g_1(r(t)) &= f_1(r(t))r^2(t) - g. \end{aligned} \quad (6)$$

To keep order α in the perturbation, in the second term in the first of (5) we can replace the actual values of r, θ by their unperturbed values $r^o(t), \theta^o(t)$. Since the unperturbed motion is completely regular, we can expand $g_1(r^o(t)) \sin 2\theta^o(t)$ in Fourier series, with basic frequencies ω_r and ω_θ

$$g_1(r^o(t)) \sin 2\theta^o(t) = \Re \left\{ \sum_{k=-\infty}^{\infty} \tilde{g}_k e^{i(k\omega_r + 2\omega_\theta)t} \right\}, \quad (7)$$

where \tilde{g}_k are certain complex coefficients. Assuming quasi-periodicity (which is the more abundant behaviour if α is small), i.e. κ irrational, we easily see from (7) that $\langle g_1 \sin 2\theta^o \rangle \approx 0$. Hence if we average the first in (5) over several radial periods we see that (see below)

$$\mathcal{K} = \frac{p_\theta^2}{2} - \Omega^2 \cos 2\theta, \quad \Omega^2 = \frac{\alpha}{2} g > 0, \quad (8)$$

is an approximate invariant. \mathcal{K} plays the role of the total energy in a simple pendulum model where Ω is the small oscillation frequency. Therefore two critical values of \mathcal{K} exist: $-\Omega^2$ and Ω^2 . For $\mathcal{K} = -\Omega^2$, $(\theta, p_\theta) = (0, 0)$ is a stable equilibrium point: the motion is stable along the x axis. On the other hand, for $\mathcal{K} = \Omega^2$ we have the separatrix and the unstable equilibrium points are $(\theta, p_\theta) = (\pm\pi/2, 0)$: the motion along the y axis is unstable. The domain of box orbits, that oscillate about the long-axis, corresponds to $|\mathcal{K}| < \Omega^2$ and the domain of loop orbits, that rotate about the origin, to $\mathcal{K} > \Omega^2$. The separatrix, $p_\theta^s = \pm 2\Omega \cos \theta^s$, separates then different kinds of motion: oscillations and rotations; i.e. box and loop orbits. For $\mathcal{K} \gg \Omega^2$, $\mathcal{K} \approx p_\theta^2/2$: the kinetic energy in the tangential direction. The largest value of \mathcal{K} corresponds to the largest p_θ , which appears for the 1:1 periodic orbit. For $V_1 \neq 0$ this periodic orbit should not be circular but elliptic with small eccentricity (see below).

Since Ω is a measure of the amplitude of the torque, we conclude that the relevant parameter that defines the orbital family is the relative value of the rotational energy

with respect to the strength of the torque, which in turn depends on the degree of flatness of the potential.

From the above discussion it turns out that a limit angle, θ_1 , could exist

$$\cos 2\theta_1 \approx -\frac{\mathcal{K}}{\Omega^2},$$

which is another way to conclude that $|\mathcal{K}| < \Omega^2$ for boxes. However it is important to remark that this bound for θ appears for r bounded away from 0. When p_θ is small, which is the case for boxes, the analysis of the motion in a neighbourhood \mathcal{R} of $r = 0$ should be done in a different way since the origin is a singular point in this description. As we assume that the potential is regular at $r = 0$, we can approximate $\phi(x, y)$ by a harmonic oscillator in \mathcal{R} . The approximate invariants of motion are then the energy in each degree of freedom h_x, h_y . But the Lissajous-like orbits in a harmonic oscillator with incommensurable frequencies are dense in \mathcal{R} whenever $h_x, h_y \neq 0$, so no bound for θ exists while the star is in \mathcal{R} .

The frequency Ω , depends on the average $\langle f_1(r)r^2 \rangle$ over the unperturbed motion (Eqs. (6) and (8)). As defined in (2), $f_1(r)$ can be put in terms of the circular speed, v_c : $f_1(r) = v_c^2(r)/2$. So from (8) follows that

$$\Omega^2 = \frac{\alpha}{4} \langle v_c^2(r)r^2 \rangle.$$

For the realistic case of flat rotation curves at large radii we get

$$\Omega^2 \approx \frac{\alpha}{4} v_c^2 \langle r^2 \rangle \sim \frac{\alpha}{12} v_c^2 r_M^2 (1 + \beta + \beta^2), \quad (9)$$

where $0 \leq \beta = r_m/r_M \leq 1$, and $r_M > r_m$ are the two roots of the equation (see Eq. (3))

$$(p_\theta^0)^2 - 2r^2 (h_0 - \Phi(r^2)) + \frac{1}{2} \alpha \Phi'(r^2) r^4 = 0,$$

which, for r_M , can be approximated by

$$(p_\theta^0)^2 - 2r_M^2 (h_0 - \Phi(r_M^2)) + \frac{1}{2} \alpha v_c^2 r_M^2 \approx 0. \quad (10)$$

For the estimate in (9), where a factor 2 should be added if $\beta = 0$, we approximate the time-average of r^2 by the r -average over the allowed interval. This is not true in general but it provides a rough estimate of the average that will help us later.

The invariant \mathcal{K} is in some sense local, since unperturbed orbits with different angular momentum will have different values of the frequency: $\Omega = \Omega(h_0, p_\theta^0)$. From (9) and (10) it is not difficult to conclude that the largest Ω is expected for minimum $|p_\theta^0|$; $p_\theta^0 = 0$, i.e., for radial orbits, while the smallest one for maximum $|p_\theta^0|$, i.e., for circular orbits (see also Sect. 2.2).

For the case of the 1:1 periodic orbit we can write,

$$\Omega_{1:1}^2 \approx \frac{\alpha}{4} v_c^2 a^2, \quad (11)$$

where a is the circular radius defined by

$$\Phi(a^2) \approx h_0 - \left(1 + \frac{\alpha}{2}\right) \frac{v_c^2}{2}. \quad (12)$$

Then, the maximum value of \mathcal{K} lies somewhere between

$$\frac{v_c^2 a^2}{2} (1 - \alpha/2) \lesssim \mathcal{K}_M \lesssim \frac{v_c^2 a^2}{2} (1 + \alpha/2) \quad (13)$$

$$(2/\alpha - 1) \Omega_{1:1}^2 \lesssim \mathcal{K}_M \lesssim (2/\alpha + 1) \Omega_{1:1}^2.$$

The whole picture given above is true for small α (q close to 1). Indeed, this approach makes sense when the x -axis periodic orbit is stable. It is well known, that for large values of α ($\alpha \sim 1$, $q \sim 0.7$) the latter orbit could become unstable bifurcating to another periodic orbit. A sub-family associated to this new orbit appears. It is expected also that the x -axis periodic orbit lies now in a narrow stochastic layer around the separatrix of the resonance (see below). Other high-order resonances would occupy some region of the phase space and many zones of stochastic motion would also appear. So it is hard to speak then only about box or loop orbits when the perturbation is large (in fact, the term boxlets is often used in this case, see for example, MS89). We refer to Sect. 5, where a global study of the logarithmic potential reveals that this ‘‘very chaotic’’ panorama does not show up even for large values of h and α . Nevertheless, in general, bounds to the value of q would appear: $0 < q_0 \leq q \leq 1$. This bound comes from the Poisson equation, $\nabla^2 \phi = 4\pi G\rho$ with $\rho > 0$.

One should remark that \mathcal{K} given by (8) was obtained neglecting high order terms, assuming quasiperiodicity in the unperturbed motion and averaging to zero the oscillating part. Thus the pendulum model is a rough first approximation to the dynamics and other perturbing terms should be present. However, the main effect of perturbations to the pendulum is to distort somehow the invariant curves and to give rise to a stochastic layer around the separatrix. That is, box and loop should be actually separated by a stochastic layer instead of a separatrix. The larger the strength of the perturbation, the larger is the width of the layer (for details about the dynamics of the pendulum model and perturbation effects, see Chirikov 1979).

The derivation given above for \mathcal{K} is a justification of the invariant introduced ad-hoc to compute certain models of elliptical galaxies that respect a third integral. Indeed, if the potential has the form

$$\phi(\mathbf{r}) = \psi(r) + \frac{\chi(\theta)}{r^2}, \quad (14)$$

with ψ and χ arbitrary functions, then a third integral exists

$$I_3 = \frac{p_\theta^2}{2} - \chi(\theta).$$

The form (14) is a particular case of a more general type of potentials introduced almost one century ago by Eddington (1915) to study oblate distributions where the ellipsoidal velocity law is exactly satisfied (he showed, however, that the latter condition does not hold if in (14) $\chi \neq 0$). Later on, this model was adopted, for instance, by Lynden-Bell (1967) in his investigations on statistical mechanics of violent relaxation in rotating elliptical systems. As was pointed out by Eddington, Lynden-Bell and

others, (14) is unsuitable for any galactic potential so, in general, the third integral for a more realistic model is supposed to be

$$I_3 = \frac{p_\theta^2}{2} - \xi(r, \theta),$$

where $\xi(r, \theta)$ is such that I_3 should satisfy approximately the collisionless Boltzmann equation (see Petrou 1983a,b for more details). No other explicit integral can be expected for a general potential of the form $\phi(r, \theta) = \psi(r) + Q(r)\chi(\theta)$.

Note, however, that for a bar-like galaxy the multipole expansion of $\phi(\mathbf{r})$ has as dominant terms

$$\phi(\mathbf{r}) \approx \psi(r) + Q(r)P_2(\cos \theta) \equiv \psi_1(r) + Q_1(r) \cos 2\theta,$$

where $P_2(\mu)$ is the Legendre polynomial of degree 2. If ψ and Q are regular at $r = 0$ we recover the Hamiltonian (3) taken as a model for the above discussion.

2.2. Example using the 2D logarithmic potential

The logarithmic potential has the form:

$$\phi(x, y) = \frac{1}{2}p_0^2 \ln(x^2 + y^2/q^2 + r_c^2) \quad (15)$$

where p_0^2 is a constant and r_c , the core radius, plays the role of a softening parameter to avoid the singularity at the origin. Hence ϕ is regular at $r = 0$ and, in \mathcal{R} defined as $r \ll r_c$, $\phi(x, y) \sim x^2 + y^2/q^2$. The circular speed is $v_c^2 \sim p_0^2$ for $r \gg r_c$ and in what follows we set $p_0^2 = 2$, $r_c = 0.1$ (see, however, next section). The semiaxis ratio, q , can take any value within the range $q_0 \leq q \leq 1$ where $q_0^2 = 1/2 - r_c^2/\exp(2h/p_0^2)$, being h the energy level. Note that q is the semiaxis ratio of isopotential curves. The semiaxis ratio for isodensity curves, \tilde{q} , is related with q by $\tilde{q} \approx q\sqrt{2q^2 - 1}$ for $r \gg r_c$ (see BT87), so isodensities are always much flatter than isopotentials. Typical orbits and their corresponding surfaces of section for this potential may be found elsewhere, for instance, BT87, MS89, PL96. In particular, the level $h = -0.4059$ is adopted hereafter following PL96 (see, however, Sect. 5). For the latter value of h , $q_0 \approx 0.696$ and the frequency of the long-axis and 1:1 (circular if $q = 1$) periodic orbits are about 2 and 3 respectively (see PL96).

As we showed in the previous section, one of the main differences between loop and box orbits is that the latter pass through the origin (projected on the configuration space, the (x, y) -plane) while the former do not. Since for boxes $|\mathcal{K}| \leq \Omega^2$, $p_\theta = 0$ is a suitable choice for the initial angular momentum for that orbits, while $\mathcal{K} > \Omega^2 \rightarrow |p_\theta| > 2\Omega$ is enough to ensure a loop orbit (see Eq. (8) and discussion below). In Cartesian variables, since $p_{\theta_0} = x_0 p_{y_0} - y_0 p_{x_0}$, in any case we can set, for instance, $y_0 = 0$ and then $p_{x_0} = 0$ for loops and $x_0 = 0$ for boxes. Therefore, for the energy level h , x_0 and p_{x_0} parameterize, respectively, loop and box orbits. The same applies if we exchange $x_0, p_{x_0} \leftrightarrow y_0, p_{y_0}$. This choice

of a single Cartesian variable to label orbits in each family will help us later (Sect. 4.2), but to investigate the connection between the actual motion and the pendulum model, we will proceed with polar coordinates.

A suitable map that should reveal the dynamics in the tangential direction is a (θ, p_θ) section for constant r and, for instance, with $p_r > 0$. Nevertheless one should ensure that the trajectory actually intersects this surface. We expect that box orbits always cross any surface $r = r_s$ provided that $r_m < r_s < r_M$. However, this is not the case for all loop orbits. For instance, in the limiting case when $q \rightarrow 1$, the 1:1 periodic orbit becomes circular and it is fully contained in $r = a$. Another restriction is that $r_s > r_c$ because, as mentioned, for $r \ll r_c$, \mathcal{K} is not well defined.

In Fig. 1 we show (θ, p_θ) surfaces of section for $r_s = 0.5$ and three different values of q , 0.9, 0.8 and 0.7. Note that for these values of q , the corresponding values of α are not small, 0.234, 0.562 and 1.04 respectively. Nevertheless the global motion resembles a pendulum model. The origin corresponds to the long-axis periodic orbit while the unstable points $(\pm\pi/2, 0)$ to the short-axis periodic orbit. The outermost curves correspond to loop orbits relatively close to the 1:1 periodic orbit (for both senses of rotation). Indeed, from (12) one immediately finds that for this orbit $a \approx 0.45, 0.42, 0.38$ for $q = 0.9, 0.8, 0.7$ respectively. Because $V_1 \neq 0$, a gives an estimation of the mean value of the semiaxis of this elliptic orbit (see Sect. 4.2 for a more accurate determination).

From Fig. 1 we see that box and loop families are separated by a relatively narrow stochastic layer and, for large values of the angular momentum, the latter is nearly an integral of motion. As q decreases from 0.9 the departures of the actual motion from the pendulum model become significant. For instance, for $q = 0.7$ we observe that the x -axis periodic orbit becomes unstable and a bifurcation to a 2-periodic orbit appears (see footnote at the end of next section). This sub-family of box family is conformed by the well-known banana orbits (see, for instance, MS89). Note the thin chaotic layer that separates bananas and boxes. We distinguish several resonances and a comparatively large stochastic layer separates boxes and loops. Some small islands are also present in the loop domain. Nevertheless, only a few loop orbits appear in this figure ($q = 0.7$) because almost all the intersections with the surface $r_s = 0.5$ correspond to box orbits. Anyway the domain of box family increases against that of loops as the flatness of the potential increases.

In Fig. 2 we show the computed values of Ω (actually Ω^2) for several (about 1500) orbits with initial conditions along the p_θ axis. We average $\Phi'(r^2)r^4 = r^4/(r^2 + r_c^2)$ over 1500 units of time which is ~ 500 periods of the x -axis periodic orbit, using the values of r obtained by solving the equations of motion corresponding to (15) with $q = 0.9, 0.8, 0.7$. We checked that the oscillating part, $g_1(r(t)) - \text{see Eq. (6)} - \text{averages to zero. For } q = 0.9 \text{ and } 0.8 \text{ almost}$

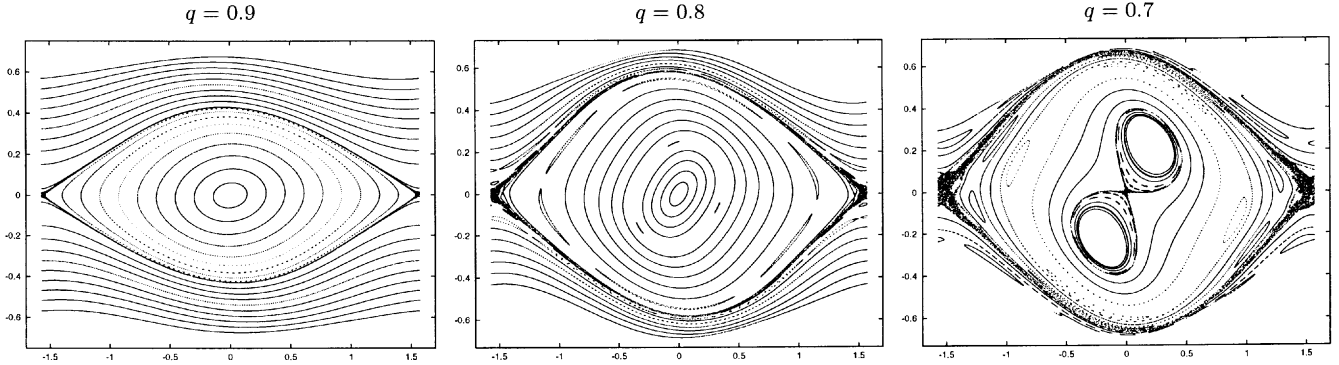


Fig. 1. Surfaces of section (θ, p_θ) , $r_s = 0.5$, $p_r > 0$ for θ restricted to the interval $(-\pi/2, \pi/2)$ and for several orbits in the logarithmic potential (15) with $r_c = 0.1$, $p_0^2 = 2$, $h = -0.4059$ and $q = 0.9, 0.8$ and 0.7 (see text for details)

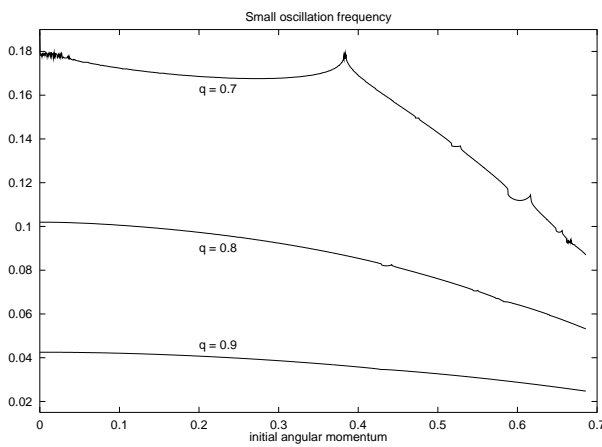


Fig. 2. Ω^2 vs. p_{θ_0} for several orbits with $r_0 = 0.5$, $\theta_0 = 0$ and $r_c = 0.1$, $h = -0.4059$. The small oscillation frequency was computed as $\Omega^2 = 0.5\alpha\langle\Phi'(r^2)r^4\rangle = 0.5\alpha\langle r^4/(r^2 + r_c^2)\rangle$ over $t \approx 500$ periods and using the actual r values (see text)

all orbits are either box or loop while for $q = 0.7$, those for $p_{\theta_0} \lesssim 0.4$ belong to the banana sub-family (see Fig. 1). In any case Ω^2 does not change too much over the whole range, less than by a factor 2. This variation of Ω can be computed using (9), (10), (11) and (12). It is immediate that the change in Ω^2 from radial ($p_\theta = 0$) to circular (maximum p_θ) orbits is

$$\frac{\Delta\Omega^2}{\Omega_{1:1}^2} \sim \frac{2}{3} \frac{r_M^2(0)}{a^2} - 1, \quad \frac{r_M^2(0) + r_c^2}{a^2 + r_c^2} \approx e^{p_0^2/2},$$

which for $r_M(0), a \gg r_c$ and $p_0^2 = 2$ leads to $r_M^2/a^2 \sim e$ and then $\Delta\Omega^2/\Omega_{1:1}^2 \sim 0.8$.

From this figure, for $q = 0.9$ and 0.8 we see a similar, smooth behaviour of Ω , except in those narrow intervals where a small island seems to be present. Since the width of the stochastic layer for these two values of q is rather small (particularly due to the fact that we are crossing the layer through the thinnest part), almost no evidence of its existence could be inferred from the figure. However for $q = 0.7$, Ω looks noisy in the vicinity of the long-axis periodic orbit as well as on the separatrix, revealing the

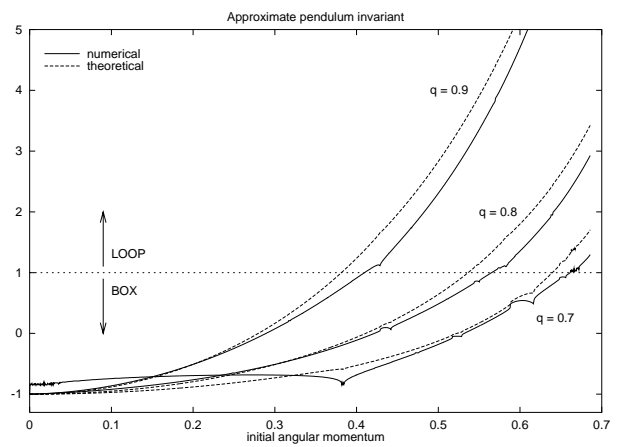


Fig. 3. \mathcal{K}/Ω^2 vs. p_{θ_0} for the same ensemble of orbits than in Fig. 2. The line $\mathcal{K}/\Omega^2 = 1$ separates the domains of box and loop orbits. The theoretical invariant for the whole ensemble, defined by $\theta_0 = 0$, was computed as $\mathcal{K}_T = p_{\theta_0}^2/2 - \Omega^2$. The numerical invariant was averaged, for each orbit, over $t \approx 500$ periods (see text)

existence of chaotic zones. Much more discontinuities can be also observed, certainly due to the existence of many resonances. For the banana family, as expected, the behaviour is different. In the latter case Ω is almost constant in all this range. This can be understood looking back to Fig. 1 and recalling that we are taking initial conditions along the p_θ axis; in all cases the banana orbits are close to the marginal one.

Having the small oscillation frequency we compute \mathcal{K} . First we took a set of representative orbits and we studied the time evolution of \mathcal{K} . We observed a nearly constant value of \mathcal{K} but, for box orbits, a periodical peak structure was observed. This was not the case for loop orbits. These peaks are due to the fact that \mathcal{K} is not an invariant when $r < r_c$; all of them appeared at minimum r . To reduce

their effect on the instantaneous value of the invariant, we averaged \mathcal{K} over the whole time interval. This procedure, however, leads to slightly larger values of \mathcal{K} due to the cumulative effect.

In Fig. 3 we show the computed values of \mathcal{K}/Ω^2 for the same ensemble of orbits than in Fig. 2. For the long-axis periodic orbit $\mathcal{K} = -\Omega^2$ (a zoom around $p_{\theta_0} = 0$ reveals that the initial value of $\mathcal{K}/\Omega^2 = -1$ also for $q = 0.7$). The line $\mathcal{K} = \Omega^2$ separates box and loop domains and a simple comparison with Fig. 1 shows that the separatrix (to be precise, the stochastic layer) is very close to that line. The maximum value observed for \mathcal{K} is, in all cases, within the interval derived in (13).

Figure 3 is illustrative to show which family dominates the dynamics at given level of energy and to identify other sub-families of the principal ones. For instance, for $q = 0.9$ box and loop orbits populate the phase space and no other sub-family seems to be significant. On the other hand for $q = 0.7$ almost all the phase space is filled by box orbits but the banana family occupies a fraction of the phase space (see Sect. 4.2). Loops are scanty and some chaotic domains seems to become important. Recall that the actual volume of the phase space occupied by any of these families would not be measured by the size of the corresponding \mathcal{K} intervals. We also include in Fig. 3 the theoretical value of \mathcal{K} which, for the ensemble considered, is $\mathcal{K}_T = p_{\theta_0}^2/2 - \Omega^2$, where we take for Ω the computed values given in Fig. 2. Note the good agreement between \mathcal{K} and \mathcal{K}_T for loops and boxes but, of course, they differ for the banana sub-family.

In Fig. 4 we show the surfaces of section, (θ, p_θ) , computed using \mathcal{K}_T and Ω obtained numerically. A comparison with Fig. 1 reveals that the actual motion is well approximated by a pendulum model for $q = 0.9$ and for $q = 0.8$, but the agreement is not so good, as expected, for $q = 0.7$.

3. Scalings and alternative presentations

In this section we shall concentrate on some geometrical remarks concerning the Hamiltonian corresponding to the logarithmic potential

$$H(\mathbf{p}, \mathbf{x}) = \frac{\mathbf{p}^2}{2} + \frac{p_0^2}{2} \ln(x^2 + y^2/q^2 + r_c^2), \quad (16)$$

where $\mathbf{x} = (x, y)$, $\mathbf{p} = (p_x, p_y)$. Along the paper, for the numerical examples, the parameters were taken as $p_0^2 = 2$, $r_c = 0.1$, $h = -0.4059$ and $0.696 < q < 1$ (Sects. 2.2 and 4.2). First of all let us mention that the parameters p_0 and r_c are not essential. Indeed, scaling to new variables $\mathbf{X} = (X, Y)$, $\mathbf{P} = (P_X, P_Y)$ by $\mathbf{x} = \beta_1 \mathbf{X}$, $\mathbf{p} = \beta_2 \mathbf{P}$ and using a new time variable $s = \gamma t$ the resulting equations of motion correspond to the Hamiltonian

$$\hat{H}(\mathbf{P}, \mathbf{X}) = \frac{\mathbf{P}^2}{2} + \frac{1}{2} \ln(X^2 + Y^2/q^2 + 1) \quad (17)$$

if $\beta_1 = r_c$, $\beta_2 = p_0$, $\gamma = p_0/r_c$. So, the energy moves to $h \rightarrow h/p_0^2 - \ln r_c \equiv \hat{h}$. This transformation is, in fact, a generalized canonical one. The energy is scaled in such a way

that the value of \hat{H} at the origin is 0. Only the energy and q are necessary to study the full family defined by (17). Alternatively, one can use r_c as a parameter keeping h fixed, for instance $h = 0$ as MS89 do (see also Appendix). From now on, in this section, we shall work with (17).

Next we study the problem of representation of the phase space. From (17) we note that for all $\hat{h} \geq 0$, $\hat{H}(\mathbf{P}, \mathbf{X}) = \hat{h}$ defines a compact level of energy which can be seen as \mathbb{S}^3 . Indeed, for small $\hat{h} > 0$ one can keep the dominant terms

$$\frac{1}{2}(P_X^2 + P_Y^2 + X^2 + Y^2/q^2) \approx \hat{h}.$$

Introducing the variables

$$x_1 = \frac{X}{\sqrt{2\hat{h}}}, \quad x_2 = \frac{Y}{q\sqrt{2\hat{h}}}, \quad x_3 = \frac{P_X}{\sqrt{2\hat{h}}}, \quad x_4 = \frac{P_Y}{\sqrt{2\hat{h}}},$$

we obtain $\sum_{i=1}^4 x_i^2 = 1$.

Now let us pass to general values of \hat{h} . Denote by $\rho^2 = X^2 + Y^2/q^2$ and define $\tilde{\rho} = \sqrt{\ln(1 + \rho^2)}$ which is analytic for any $\rho > 0$. Then we introduce

$$x_1 = \frac{X\tilde{\rho}/\rho}{\sqrt{2\hat{h}}}, \quad x_2 = \frac{Y\tilde{\rho}/\rho}{q\sqrt{2\hat{h}}}$$

and x_3, x_4 as above, so $\sum_{i=1}^4 x_i^2 = 1$.

A simple way to use these variables is as follows. All orbits intersect transversally, for instance, $y = 0$ except the x -axis periodic orbit which is always contained on this plane and appears as the boundary of this surface of section, $x_1^2 + x_3^2 = 1$ or $P_X^2 + \ln(1 + X^2) = 2\hat{h}$ – see Fig. 5. One can identify the points in the boundary to a single point. Points (x_1, x_3) such that $x_1^2 + x_3^2 < 1$, represent an open disc so that, identifying the boundary to a single point, we obtain a 2D sphere \mathbb{S}^2 . By definition we send the origin $(x_1, x_3) = (0, 0)$ to the south pole (SP) and the boundary $x_1^2 + x_3^2 = 1$ to the north pole (NP). As it could be also used the section $x = 0$ and because in this case the boundary corresponds to the y -axis periodic orbit, $x_2^2 + x_4^2 = 1$, we are interested in doing the mentioned identification with suitable symmetry properties.

Given, for instance, x_1 and x_3 on the section through $y = 0$, we define the angles $0 \leq \varpi \leq \pi/2$ and $0 \leq \lambda < 2\pi$ as (see Fig. 5)

$$\sin \varpi = \sqrt{x_1^2 + x_3^2}, \quad \tan \lambda = \frac{x_3}{x_1}, \quad (18)$$

such that, on \mathbb{S}^2 , 2ϖ is the polar angle measured from the SP while λ is the usual azimuthal angle. Then introducing Cartesian coordinates (ξ, η, ζ)

$$\xi = \sin 2\varpi \cos \lambda, \quad \eta = \sin 2\varpi \sin \lambda, \quad \zeta = -\cos 2\varpi \quad (19)$$

we get the desired representation. This transformation is similar to the use of a Hopf fibration of \mathbb{S}^3 (see Stiefel & Scheifele 1971).

Hence the “natural” space to represent the full dynamics is \mathbb{S}^2 . Periodic orbits along the axes appear at the poles and the “pendulum-like oscillations” for loops

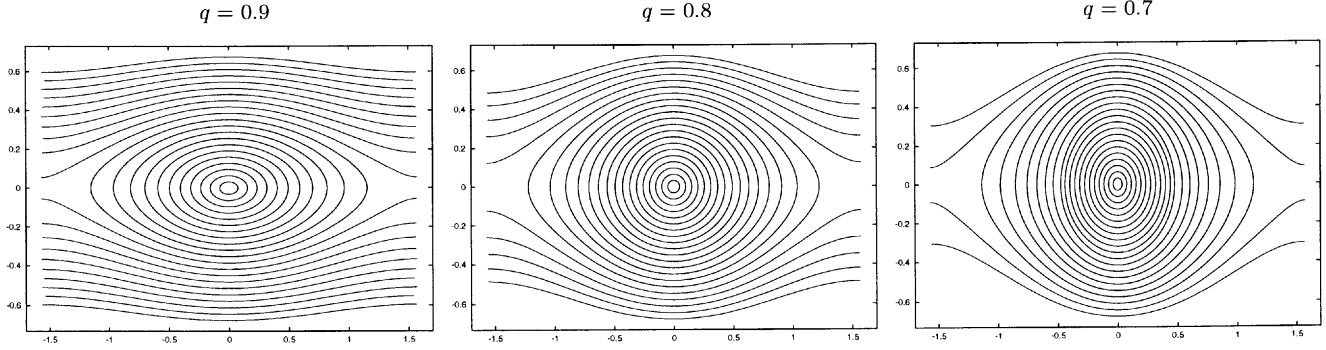


Fig. 4. Theoretical surfaces of section (θ, p_θ) for $q = 0.9, 0.8$ and 0.7 computed using \mathcal{K}_T and Ω obtained numerically. Compare with Fig. 1

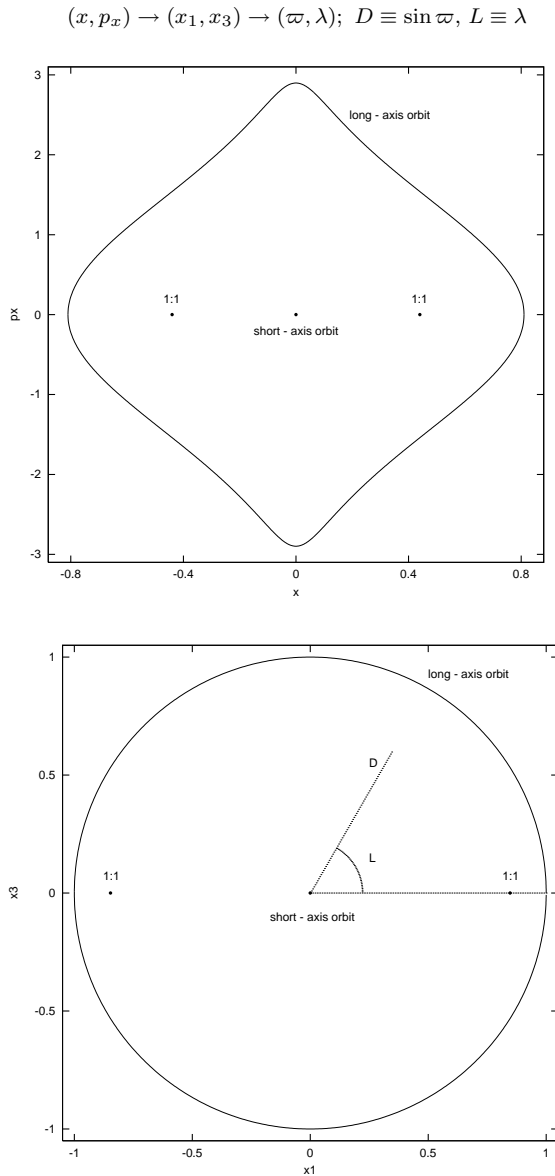


Fig. 5. Sketch of the transformation from the xp_x to x_1x_3 -plane and to angles (ϖ, λ) . The section was drawn for the Hamiltonian (16) with $h = -0.4059, q = 0.9, r_c = 0.1, p_0^2 = 2$

fit on this sphere. One can also understand this representation by looking back to Fig. 1 or Fig. 4. Points with $\theta = -\pi/2$ and $\pi/2$ are identified. In this way we obtain a cylinder. Then points on the upper curve (1:1 direct periodic orbit) are identified to a single point, as well as points on the lower curve (1:1 retrograde periodic orbit). The cylinder becomes \mathbb{S}^2 and then it is turned to have $(0, 0)$ and $(0, \pi/2)$ at the SP and NP respectively. But note that in this case the pendulum oscillations, as described in Sects. 2.1 and 2.2, correspond to boxes.

For completeness we list the transformation in case the formulation (16) is desired. Let then, for instance, (x, p_x) be the values in the $y = 0$ surface of section with, say, $p_y > 0$, unless we are at the boundary. Compute first $X = x/r_c, P_X = p_x/p_0, \hat{h} = h/p_0^2 - \ln r_c$ and then

$$x_1 = \text{sign}(X) \frac{\sqrt{\ln(1 + X^2)}}{\sqrt{2\hat{h}}}, \quad x_3 = \frac{P_X}{\sqrt{2\hat{h}}}. \quad (20)$$

Having x_1 and x_3 , (18) and (19) give us (ξ, η, ζ) . A similar transformation follows for (y, p_y) in the $x = 0$ section.

Figure 6 displays, for $q = 0.75, r_c = 0.1$ and $h = -0.4059$ (similar to Fig. 1 (right) but for different variables) the cross section $x = 0$. The NP, that for this section corresponds to the unstable y -axis orbit, is seen as an hyperbolic point inside a gross stochastic layer. The SP, that corresponds to the x -axis orbit, also appears as an hyperbolic point, because for this value of q the latter orbit is unstable. Note the 2-periodic orbit³ that bifurcates from the x -axis orbit that gives rise to the banana orbits. The other elliptic points on the northern hemisphere correspond to the 1:1 periodic orbit (direct and retrograde). Therefore “pendulum-like” oscillations correspond to loops while rotations to boxes. In other words, for boxes, λ ranges from 0 to 2π while for loops, λ is confined to some subinterval of $[0, 2\pi)$. For a better visualization, orbits in the “hidden” part of the sphere (SP and almost all the southern hemisphere) were drawn with much less points.

³ This orbit has two intersections with the xp_x -plane, due to its shape, but only one with the yp_y -plane. In any case it is not obtained by period doubling.

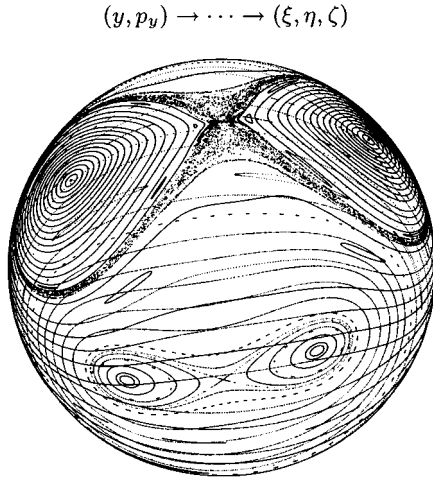


Fig. 6. Surface of section $x = 0$ on the sphere $\xi^2 + \eta^2 + \zeta^2 = 1$, for the Hamiltonian (16) with the same parameters than Fig. 5 but $q = 0.75$. The “hidden” part was drawn with less points

4. Measure of chaos and fine structure of the phase space

4.1. The Mean Exponential Growth factor of Nearby Orbits (MEGNO)

In Sect. 2 we have shown that if the potential is not too far from the central symmetry, we can derive the global orbital structure by means of an additional pseudo-invariant. With this model we cannot describe chaotic zones (like the stochastic layer that separates box and loop families) and secondary resonances (like the banana sub-family). Hence to get information about the fine structure of the phase space as well as to measure chaos in the irregular components we should follow some other approach. As we pointed out in Sect. 1 the LCN provides a good measure of chaos but it does not furnish any information about the structure of the regular component. This fact is a consequence of the definition of the LCN, σ , for a given orbit, $\gamma(t)$, on a compact energy surface, M_h ,

$$\sigma(\gamma) = \lim_{t \rightarrow \infty} \frac{1}{t} \ln \frac{\delta(\gamma(t))}{\delta_0}, \quad (21)$$

(if the limit exists) where $\delta(\gamma(t)) \equiv |\boldsymbol{\delta}(\gamma(t))|$ and δ_0 are infinitesimal displacements from γ at times t and 0, respectively. $\boldsymbol{\delta}(\gamma(t))$ satisfies the variational equations $\dot{\boldsymbol{\delta}} = \Lambda(\gamma(t))\boldsymbol{\delta}$, where Λ is the Jacobian matrix of the vector field.

In practice, instead of the infinite limit one computes $\sigma(\gamma(T))$ for T “large enough”, for instance, 10^4 characteristic periods. For any regular orbit, $\delta(\gamma(t)) \approx \delta_0(1 + \lambda_\gamma t)$ – see below – and then $\sigma(\gamma(T)) \approx \ln T/T$, almost independent of γ . However some departures from the latter value exist depending whether the orbit is periodic stable or it is stable quasiperiodic but passing close to an unstable periodic orbit.

As an example let us consider a neighbourhood, U , of an unstable periodic orbit γ_u . The motion in U is mainly

determined by the stable and unstable manifolds associated to γ_u . Therefore any quasiperiodic orbit, γ_q , that falls in U will mimic, for a short time interval, γ_u . Since for the latter $\delta(\gamma_u(t))$ grows exponentially with time, then $\delta(\gamma_q(t))$ will behave in a similar manner while γ_q lies in U . This will happen periodically, each time γ_q enters in U . Therefore if we look at the time evolution of $\sigma(\gamma_q(t))$ we should see a $\ln t/t$ law modulated by a periodic peak structure (besides the purely quasiperiodic oscillations). Anyway the final value of $\sigma(\gamma_q(t))$ for $t = T$ will be very close to $\ln T/T$, except (perhaps) if we stop the computation just when γ_q is in U . The only way to put in evidence the latter behaviour is to take into account somehow the time evolution of $\sigma(\gamma(t))$. A simple way to do that and to amplify the effect of unstable periodic orbits on quasiperiodic motion is the following.

The definition of the LCN, given by (21), can be written in an integral form as

$$\sigma(\gamma) = \lim_{T \rightarrow \infty} \frac{1}{T} \int_0^T \frac{\dot{\delta}(\gamma(t))}{\delta(\gamma(t))} dt \equiv \left\langle \frac{\dot{\delta}}{\delta} \right\rangle,$$

where $\dot{\delta} \equiv \dot{\boldsymbol{\delta}} \cdot \boldsymbol{\delta} / \delta$ is the time derivative of $\delta(\gamma(t))$ and $\langle \cdot \rangle$ denotes the usual time-average. Let us define the Mean Exponential Growth factor of Nearby Orbits, \mathcal{J} , as

$$\mathcal{J}(\gamma(T)) \equiv \frac{2}{T} \int_0^T \frac{\dot{\delta}(\gamma(t))}{\delta(\gamma(t))} t dt. \quad (22)$$

Then for any regular, quasiperiodic orbit, γ_r , we get

$$\mathcal{J}(\gamma_r(T)) \approx 2 \left(1 - \frac{\ln(1 + \lambda_{\gamma_r} T)}{\lambda_{\gamma_r} T} \right) + O(\gamma_r(T)), \quad (23)$$

where, as before, $\lambda_{\gamma_r} > 0$ is the linear rate of divergence in a neighbourhood of γ_r and $O(\gamma_r(T))$ denotes an oscillating term ($\langle O(\gamma_r(T)) \rangle = 0$) introduced by the corresponding quasiperiodic terms in $\delta(\gamma_r(T))$. Indeed, for stable, regular motion $\delta(\gamma(t))$ can be approximated by $\delta \approx \delta_0[1 + \lambda t + t u(t)]$ where u is an oscillating function of t and $|u(t)|$ is bounded, say $|u(t)| < b < \lambda$. So it is straightforward to show that for large T , $\mathcal{J}(\gamma_r(T))$ oscillates about 2 and when $T \rightarrow \infty$ with an amplitude

$$|\mathcal{J}(\gamma_r(T)) - 2| < 4 \ln \frac{\lambda_{\gamma_r} + b}{\lambda_{\gamma_r} - b}.$$

Hence if the motion is quasiperiodic, then $O(\gamma_r(T))$ represents eventually small oscillations around the mean value of $\mathcal{J}(\gamma_r) \equiv \mathcal{J}_r$, that can be neglected. In case γ_r is close to a periodic orbit, $O(\gamma_r(T))$ exhibits a nearly periodic character and small amplitude.

As we note from (23), λ_{γ_r} determines how fast $\mathcal{J}_r \rightarrow 2$. Since λ is a measure of the lack of isochronicity around γ (to be precise, λ is the largest eigenvalue of the matrix $\partial \boldsymbol{\omega} / \partial \mathbf{I}$, being \mathbf{I} the action), we see that the smaller λ appears for γ in a neighbourhood of a stable periodic orbit. Therefore we expect a slower rate of convergence of \mathcal{J}_r to 2 for γ_r close to a stable “elliptic” periodic orbit. On the other hand, from the discussion given above about the behaviour of quasiperiodic orbits close to unstable periodic ones, we expect that in this case \mathcal{J}_r presents

quasiperiodic oscillations, given by $O(\gamma_r(T))$, as well as a peak structure. Therefore for arbitrary γ_r , the formal limit, $\lim_{T \rightarrow \infty} \mathcal{J}(\gamma_r(T))$, does not exist (see below).

For any irregular orbit, γ_i , for which δ grows exponentially with time, we get

$$\mathcal{J}_i \equiv \mathcal{J}(\gamma_i(T)) \approx \sigma_{\gamma_i} T + \widehat{O}(\gamma_i(T)), \quad (24)$$

where σ_{γ_i} is the LCN for γ_i and $\widehat{O}(\gamma_i(T))$ is an oscillating (in general neither quasiperiodic nor periodic) term.

While \mathcal{J} has not a formal limit, \mathcal{J}/T and the mean values $\bar{\mathcal{J}}_r, \bar{\mathcal{J}}_i$ have an asymptotic law for $T \rightarrow \infty$

$$\bar{\mathcal{J}}_r \approx 2, \quad \bar{\mathcal{J}}_i \approx \sigma_i T; \quad \frac{\bar{\mathcal{J}}_r}{T} \approx \frac{2}{T}, \quad \frac{\bar{\mathcal{J}}_i}{T} \approx \sigma_i. \quad (25)$$

For regular motion $\bar{\mathcal{J}}_r$ is constant, almost independent of initial conditions and any other parameter while, for irregular motion, $\bar{\mathcal{J}}_i$ grows linearly with time with a rate that is the LCN. Note that $\hat{\sigma}_r = \bar{\mathcal{J}}_r/T$ converges faster to zero than $\sigma_r(T) = \ln T/T$, while $\hat{\sigma}_i = \bar{\mathcal{J}}_i/T$ converges to the actual non-zero LCN, σ_i , with the same rate as it does $\sigma_i(T)$ (compare Eqs. (24), (25) with (21)).

Of most importance is that $\bar{\mathcal{J}}(T)$ can be written in an unique way for both types of motion, $\bar{\mathcal{J}}(T) \approx aT + b$ with $a = 0, b = 2$ for regular, quasiperiodic motion and $a = \sigma, b = b_0 \approx 0$ for irregular one. If $\delta(\gamma(t))$ grows with some power of t , say n , as it could happen in some degenerated cases, $a = 0, b = 2n$. Only when the phase space has a hyperbolic structure, where nearby orbits diverge exponentially with time, $a \neq 0$ and the MEGNO grows with time. This occurs for irregular, chaotic motion and also, for instance, for unstable periodic orbits (see Giorgilli et al. 1997, for a visualization of the hyperbolic structure of chaotic zones).

From (25) it turns out that if we have $\mathcal{J}(T)$ for any T we can recover the LCN by a linear least squares fit. The main advantage of this approach is that we use the dynamical information contained in $\mathcal{J}(T)$ along the whole time interval. Hence, we expect that this procedure will provide a good estimation of the LCN in both regular and irregular domains. Furthermore a least squares fit will also give us information about the location of hyperbolic orbits, the very origin of chaos. Therefore the derivation of the LCN from the MEGNO seems to be useful not only to get the global dynamics but to learn some details concerning the fine structure of phase space as well. A more complete discussion about the MEGNO technique as well as some examples of application to 3D systems are given in Cincotta et al. (2000).

4.2. Application to the 2D logarithmic potential

To investigate numerically this technique we considered again the logarithmic potential defined in (15), or its associated Hamiltonian (16), for the same parameters, energy level, M_h , and q values taken in Sect. 2.2. We use the initial values x_0, p_{x_0} to parameterize loop and box orbits respectively (see Sect. 2.2 and below).

The computation of \mathcal{J} was done using (22) for a given set of initial conditions. All the integrations were carried out for a realistic time scale, $T \sim 10^3 T_D \approx 3000$ where T_D is the period of the long-axis periodic orbit. Therefore the computational effort per unit time is almost the same needed to compute the LCN but comparatively shorter motion times are required. The renormalization of δ (if necessary), proceeds naturally from (22).

To solve the variational equations we took δ_0 along the x axis for loops and along the p_x axis for boxes with $|\delta_0| = 1$ and random sign. We used a Runge-Kutta 7/8 th order integrator (the so-called DOPRI8 routine, see Prince & Dormand 1981; Hairer et al. 1987). The accuracy in the preservation of the value of the energy is $\sim 10^{-13}$.

To eliminate fast quasiperiodic oscillations, that is, to compute $\bar{\mathcal{J}}(T)$, we averaged $\mathcal{J}(T)$ as follows

$$\bar{\mathcal{J}}(T_k) = \frac{1}{k} \sum_{i=1}^k \mathcal{J}(T_i), \quad T_k = T_0 + k\Delta T, \quad (26)$$

where $\Delta T \approx 0.06$ is the time-step. Hence $\bar{\mathcal{J}}$ depends on T and weakly on ΔT . Alternatively, if necessary, $\bar{\mathcal{J}}(T)$ computed as $T^{-1} \int_0^T \mathcal{J}(t) dt$ would provide a smoother behaviour than (26), which is independent of the time step.

To perform the least squares fit to get the slope of $\bar{\mathcal{J}}(T)$, that is the LCN, we use the values of $\bar{\mathcal{J}}(T)$ along the last 85% of the time interval ($450 \leq T \leq 3000$), just to avoid the initial transient. We add a factor 2 in the derived slope to compensate the average introduced in $\bar{\mathcal{J}}$. Indeed, since for an irregular orbit \mathcal{J} grows nearly linear, the slope derived from $\bar{\mathcal{J}}$ would be underestimated in a factor 2.

In Fig. 7 we show the time evolution of $\bar{\mathcal{J}}$ for three representative orbits. The regular ones belong to the loop family while the irregular one to the stochastic layer. For the latter we plot \mathcal{J} together with $2\bar{\mathcal{J}}$ to put in evidence that the factor 2 introduced ad hoc is necessary. The figure on the left corresponds to two regular orbits, A and B. Orbit A, stable quasiperiodic, saturates very fast from below to 2, without any significant oscillation. Orbit B, also stable quasiperiodic, comes very close to an unstable periodic orbit. We observe the influence of the unstable periodic orbit on B leading to several local maxima of decreasing amplitude. This behaviour of the amplitude of the maxima is due to the average of \mathcal{J} (see Eq. (26)) and it should decrease as $\sim 1/T$. Note that in this case $\bar{\mathcal{J}}$ takes higher values. This is also due to the presence of a nearby hyperbolic orbit. For the irregular orbit, C, (on the right figure) we see a nearly linear behaviour. In fact, $\bar{\mathcal{J}}(T)$ looks smoother and follows the same linear trend than $\mathcal{J}(T)$.

In Fig. 8 we plot the time evolution of $\hat{\sigma}(T) \equiv \bar{\mathcal{J}}/T$ and $\sigma(T)$ for orbits A and C. For the regular orbit A, $\hat{\sigma}(T) < \sigma(T)$. The theoretical values (in logarithmic scale) are -3.18 and -2.57 respectively (see Eq. (25) and around), which are in good agreement with the computed

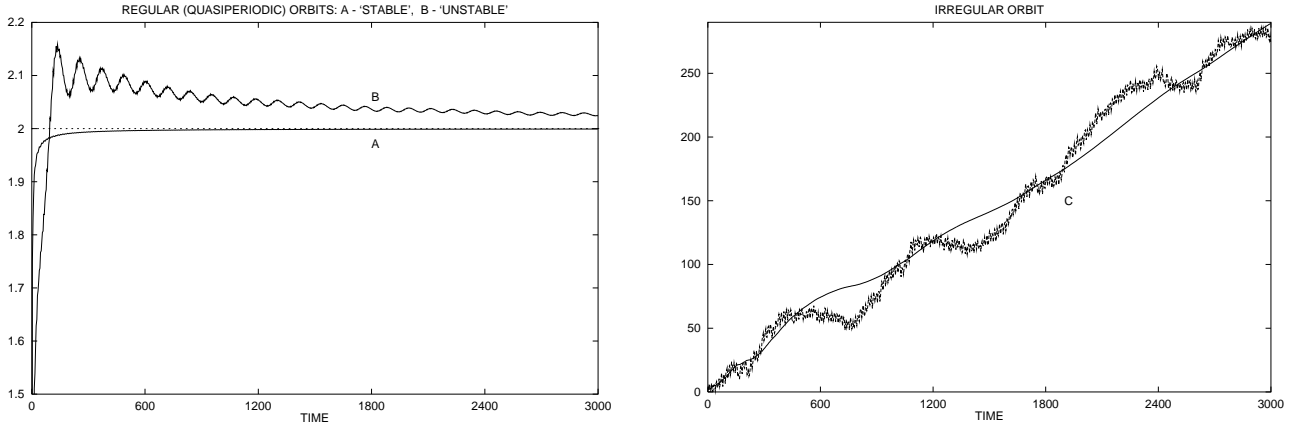


Fig. 7. Time evolution of $\bar{\mathcal{J}}$ for regular and irregular orbits. On the left, for two regular, stable quasiperiodic orbits, A, B, but orbit B is very close to a unstable periodic orbit. On the right, we plot both $\bar{\mathcal{J}}$ (smooth curve – actually $2\bar{\mathcal{J}}$, see text) and \mathcal{J} (noisy curve) for an irregular orbit, C, in the stochastic layer. All these orbits correspond to the logarithmic Hamiltonian (16) with $p_0^2 = 2$, $r_c = 0.1$, $q = 0.9$, and on the energy surface M_h defined by $h = -0.4059$ and initial conditions $x_0 \approx 0.33$, 0.02 , 0.002 , $y_0 = 0$, $p_x = 0$ for A, B and C, respectively

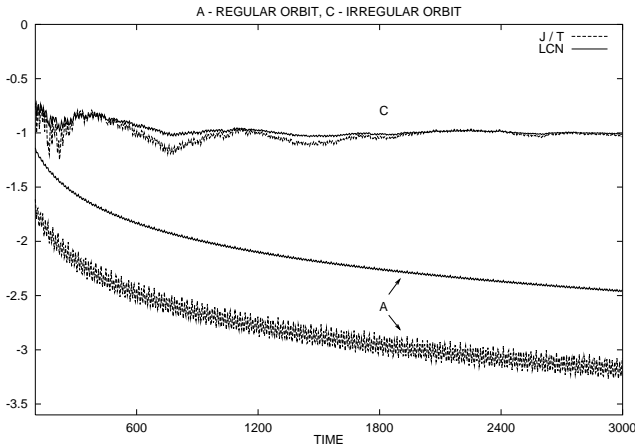


Fig. 8. Time evolution of $\log \hat{\sigma}(T)$, $\log \sigma(T)$ for orbit A, stable quasiperiodic and C, irregular, shown in Fig. 7 (see text)

ones. For the irregular orbit C, we see that $\hat{\sigma}(T) \approx \sigma(T)$, also consistent with the above discussion.

Since the relative error in the estimation of the positive LCN after a motion time T is $\sim T_L/T$, where $T_L = 1/\sigma$ is the Lyapunov time, we see that $T \sim 10^3 T_D$ is not enough to separate a chaotic region with $T_L \sim 10^3 T_D$ from the regular one. This is one of the reasons of why it is necessary to take very long motion times to compute the LCN using the standard method. It is important to remark that in this particular application it is enough to obtain an estimation of the order of magnitude of T_L . When an accurate determination of the LCN is necessary, the motion time could be very large. The presence of small resonance domains embedded in a chaotic sea produces the so-called stickiness that reduces the free diffusion. So the motion time needed in this case to compute the positive LCN should be large enough so that the orbit could fill almost all the available subset of the energy surface.

Let us now consider ensembles of orbits. To explore the phase space we use a 1D initial conditions space. The best choice would be, for instance, points along a maximum circle connecting the NP and SP of the sphere shown in Fig. 6 and passing through the 1:1 and 2:1 periodic orbits. In this way we would include loops, boxes, bananas, etc. Thus, the angle ϖ is a good parameter to label orbits in the main families. Nevertheless, to compare our results with that given by PL96 we follow their approach. Thus, for loops we take the ensemble $L_q = \{0 \leq x_0 \leq X(q), y_0 = 0, p_{x_0} = 0\} \subset M_h$ where $X(q)$ corresponds to the location along the x -axis of the 1:1 periodic orbit for a given value of q . In the same way, for box orbits, $B_q = \{x_0 = 0, y_0 = 0, 0 \leq p_{x_0} \leq P(q)\} \subset M_h$ where $P(q) \equiv P$ corresponds to the location along the p_x -axis of the long-axis periodic orbit. For the values of q considered here, one numerically finds that $X(q) \approx 0.44, 0.38, 0.33$ for $q = 0.9, 0.8, 0.7$, respectively (compare with the values derived in Sect. 2.2) while $P = (2h - p_0^2 \ln r_c^2)^{1/2} \approx 2.9$. We take ensembles of about 3500 initial conditions, similar to that considered by PL96. For each orbit we compute $\mathcal{J}(T)$, $\bar{\mathcal{J}}(T)$, $\sigma(T)$ after $T = 3000 \approx 10^3 T_D$ and we derive the slope of $\bar{\mathcal{J}}(T)$, σ_{1s} , by a least squares fit in the way described above.

In Fig. 9 we show in the same plot σ and σ_{1s} for L_q and B_q ($q = 0.9, 0.8$ and 0.7). First of all we note that in any case σ and σ_{1s} agree in the gross stochastic layer. The same happens, for $q = 0.7$, in the thin stochastic layer around the x -axis periodic orbit as well as in some narrow chaotic zones around other resonances. But the value of σ over all regular regions is nearly the same, $\log \sigma \approx \log(\ln T/T) \approx -2.57$. Just a few zones, where σ appears to behave in a smoother way, could be supposed to be the signature of an island. In contrast, σ_{1s} clearly shows the underlying structure of the regular region. Note that σ_{1s} leads to a Lyapunov time for the regular component

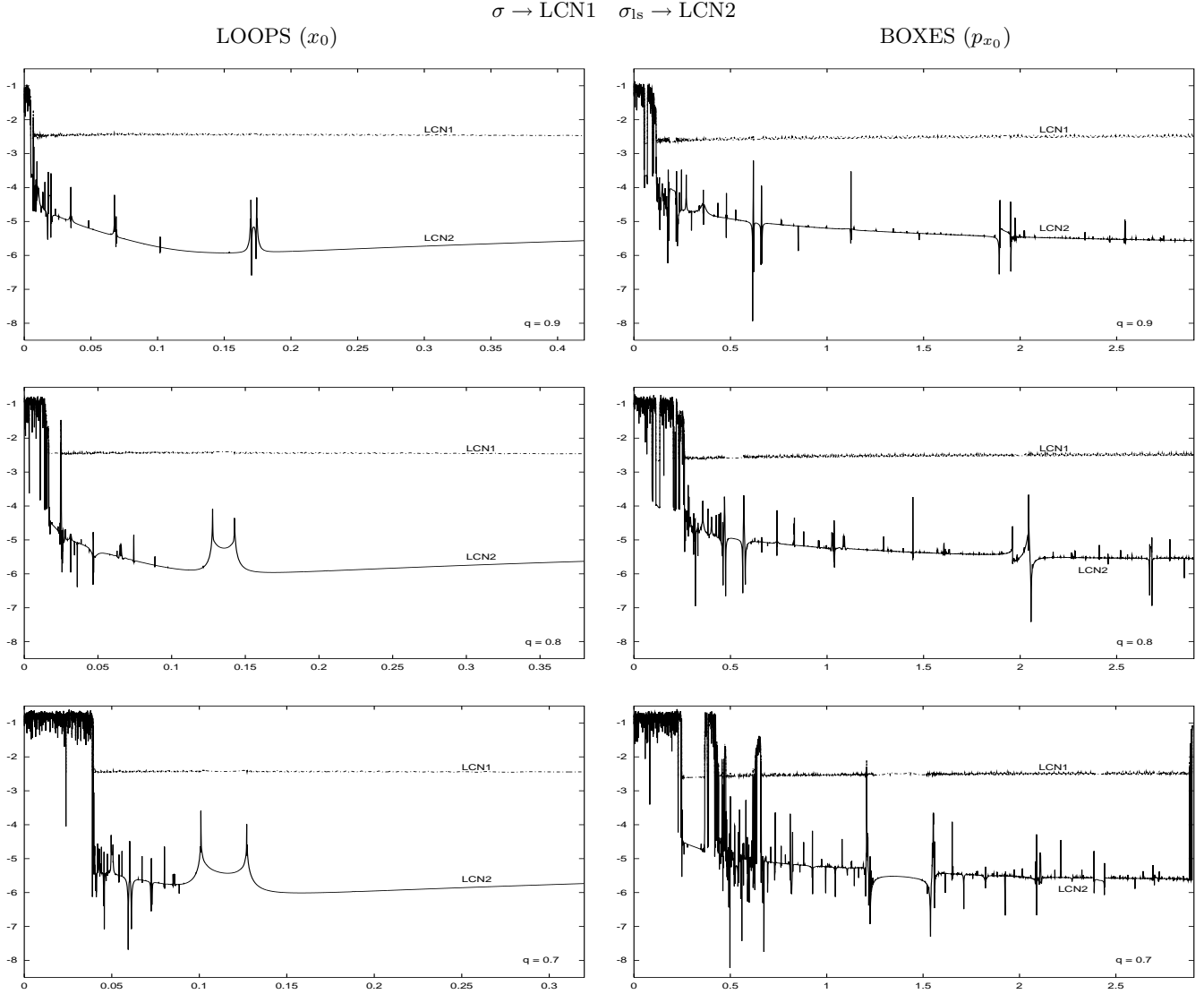


Fig. 9. $\log \sigma$, $\log \sigma_{1s}$ for the domains of loop orbits (left column) and box orbits (right column). Each point represent an orbit labeled by the initial value of x -coordinate, x_0 , for loops and the initial value of p_x -coordinate, p_{x_0} , for boxes. The ensembles include, in each case, about 3500 orbits and the total motion time is $T = 3000 \approx 10^3 T_D$ (see text for details)

of $T_L \sim 10^6 T_D$ in $10^3 T_D$ while σ leads to $T_L \sim 10^2 T_D$. To get such long values of T_L (in the regular domain) by means of the computation of σ , the total motion time should be $T \sim 10^7 T_D$.

Globally we see that, for L_q (Fig. 9 – left column), the domain is clearly divided in two zones. One near to the unstable short-axis orbit (at the origin), that contains irregular orbits and many small sub-families corresponding to each small resonance domain (see below). The other zone, near to the 1:1 periodic orbit, looks free of resonances and completely populated by quasiperiodic loop orbits. Note that σ_{1s} increases slowly as we approach to the 1:1 orbit. This is a consequence of the fact that the rate of convergence of \mathcal{J} to 2 is the slower for orbits near to the latter “elliptic” periodic orbit (see Sect. 4.1).

For B_q (right column) the scenario is different. The fraction of irregular orbits is larger (specially for q not too far from 1) and we can appreciate many resonances along the whole domain, even for $q = 0.9$. For the largest perturbation, $q = 0.7$, one could infer that quasiperiodic box orbits do exist but, in some sense, discontinuously and the region occupied by other sub-families (boxlets) is almost as large as that filled by purely box orbits. Recall that the banana sub-family is not included here because all that orbits cross the surface $y = 0$ near the boundary of the section with $x \neq 0$ (this follows immediately from Fig. 1; see also Fig. 15). As a difference with L_q , σ_{1s} decreases slowly as we approach to the long-axis periodic orbit. This behaviour is purely due to the choice of variables, since if instead of (x, p_x) we had used (y, p_y) , this orbit would appeared as an elliptic point. This effect

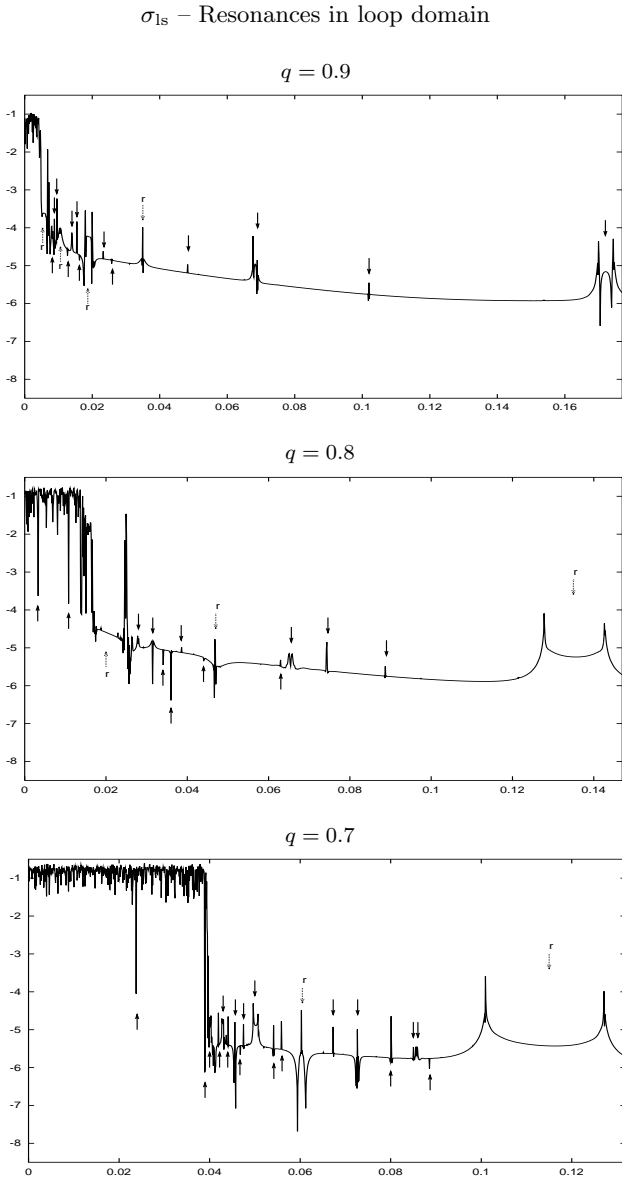


Fig. 10. $\log \sigma_{1s}$ for the region of loop domain occupied by resonances. All significant resonances are marked by a full-line arrow. Those indicated by a dashed-line arrow and labeled by “r” are also detected by PL96 by means of the FMA (see text)

is a consequence of the projection of the motion onto a 2D plane while, if we project it onto the “natural” space, which is the 2D sphere, this problem does not appear.

In Fig. 10 we plot the resonance zone for loops close to the stochastic layer. We marked by an arrow the most significant resonances. Those labeled by “r” were also detected by PL96 by means of the frequency map analysis (FMA) and therefore we have at hand the rotation number corresponding to these resonances (see Sect. 6). It is important to mention that the resolution in x_0 is similar to that of PL96 but the motion time used here is larger, about a factor 10 ($10^3 T_D$ and $10^2 T_D$, respectively). Yet, Fig. 7 shows that shorter motion times, about $500 T_D$,

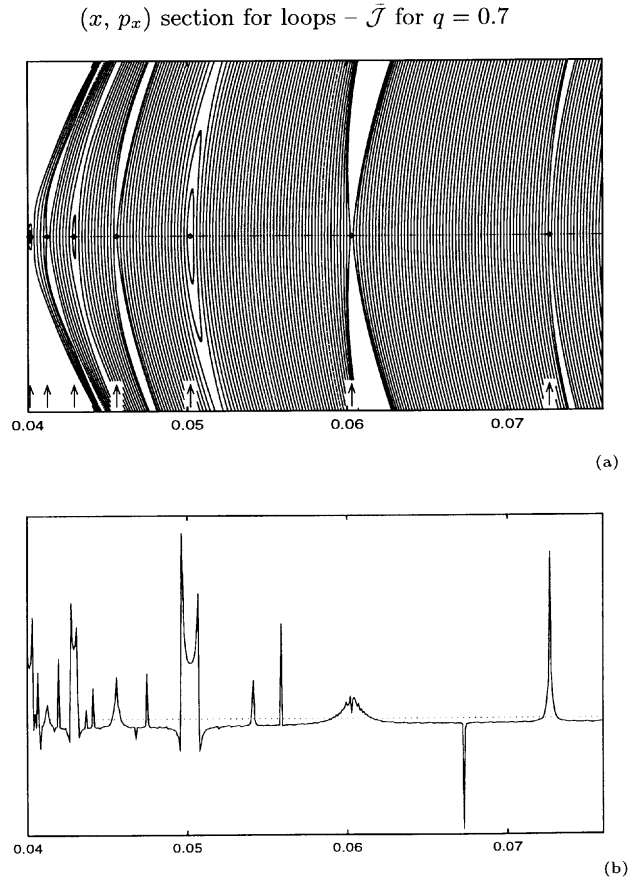
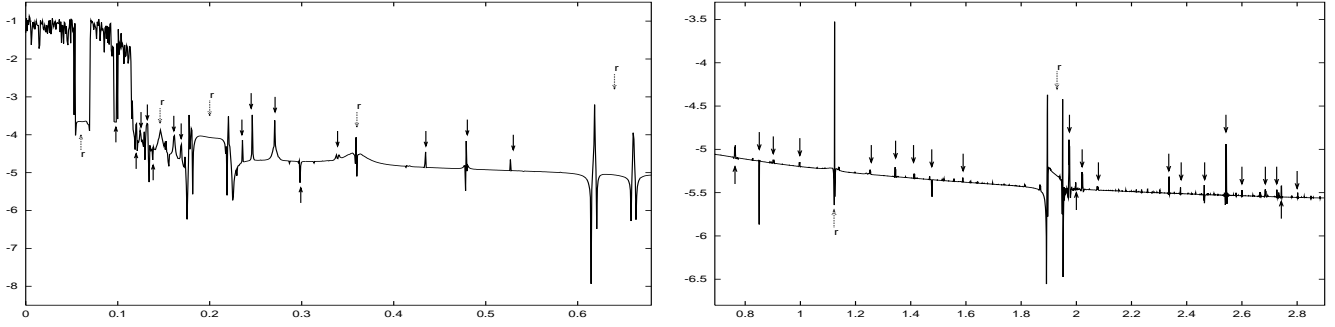


Fig. 11. **a)** Section $y = 0$ for loops close to the border of the stochastic layer, window: $0.04 \leq x \leq 0.076$, $|p_x| \leq 0.08$. The arrows indicate some of the resonances marked in Fig. 10 ($q = 0.7$) near to the stochastic layer. **b)** $\bar{\mathcal{J}}$ after $T = 3000$ and for x_0 in the same interval as above. The range in $\bar{\mathcal{J}}$ is $[1.98, 2.035]$ and the dotted line is the level $\bar{\mathcal{J}} = 2$ (see text)

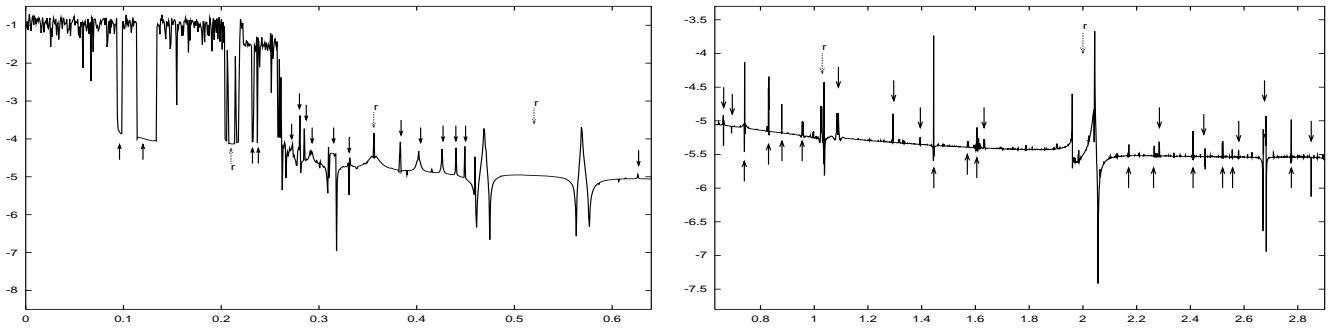
would be enough. Note that, in any case, this technique is able to put in evidence the complex structure of resonances in the neighbourhood of the stochastic layer. We distinguish basically two different types of departures from quasiperiodic motion, peaks and valleys. From the discussion given in Sect. 4.1 we easily conclude that the peaks correspond to unstable periodic orbits and to quasiperiodic orbits in a neighbourhood of the latter. The valleys appear when some orbits are locked inside a resonance. For example, looking at Fig. 10 for $q = 0.7$ we observe a single peak very close to $x_0 = 0.06$ and, for $0.1 \lesssim x_0 \lesssim 0.13$, we see two peaks at both sides of a valley. In the first case the peak is due to the fact that we are crossing an island chain through the hyperbolic point, the orbits never fall inside the resonance. On the other hand, when we cross the island chain through the center of one island, i.e. through the elliptic point, we intersect twice the separatrix and some orbits are trapped by the resonance. The width of a peak or a valley is then a measure of the actual size of the resonance.

σ_{1s} – Resonances in box domain

$q = 0.9$



$q = 0.8$



$q = 0.7$

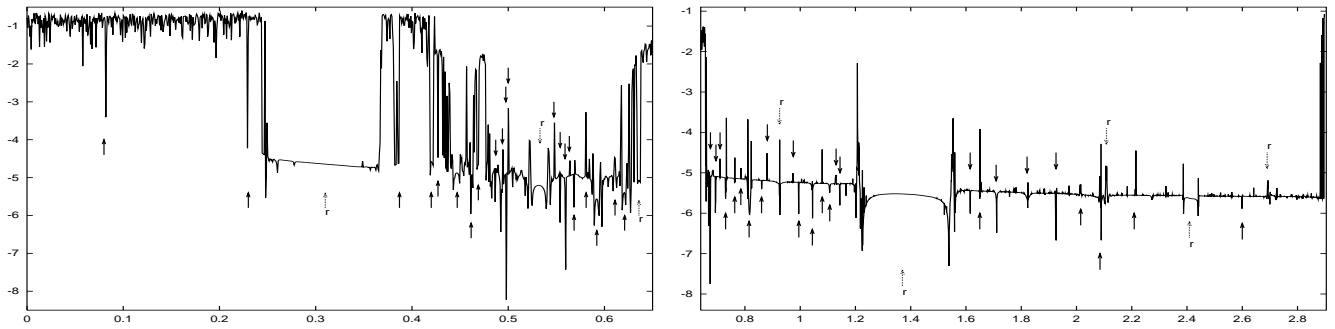


Fig. 12. $\log \sigma_{1s}$ for the whole box domain but in different windows. All significant resonances are marked by a full-line arrow. Those indicated by a dashed-line arrow and labeled by “r” are also detected by PL96 by means of the FMA (see text)

This can be visualized also from Fig. 11a where we plot a high-resolution surface of section for loops in the neighbourhood of the unstable periodic orbit at $x_0 \approx 0.06$ (4:9 resonance, see Sect. 6). The arrows in this figure indicate some of the resonances observed in the corresponding Fig. 10. In the latter figure, for $0.05 \lesssim x_0 \lesssim 0.06$ we have marked two small peaks that should correspond to unstable periodic orbits but in Fig. 11a their presence is not evident. Nevertheless for $x_0 \approx 0.055$ one can distinguish a rather narrow resonance that should be responsible of one of the mentioned peaks (in fact, to that located more distant to the 4:9 resonance). A similar picture to that given by σ_{1s} comes from $\bar{\mathcal{J}}$ where Fig. 11b is representative to illustrate the MEGNO’s behaviour. Here we plot

the final value of $\bar{\mathcal{J}}$ for the same window shown in Fig. 11a and only for ~ 400 orbits with the same resolution in x_0 like that in Figs. 9 and 10. Along this interval $\bar{\mathcal{J}}$ is very close to 2 but we can appreciate the resonances observed in the surface of section as well as those marked in Fig. 10. In any case $1.98 < \bar{\mathcal{J}} < 2.035$ and the dotted line corresponds to the theoretical value for stable quasiperiodic motion, $\bar{\mathcal{J}} = 2$.

Figure 10 as well as Fig. 12, where we plot the full domain of box family in separated windows (but with the same resolution in p_{x_0} than in Fig. 9), are very illustrative to see how resonances in the neighbourhood of the stochastic layer overlap as the perturbation increases,

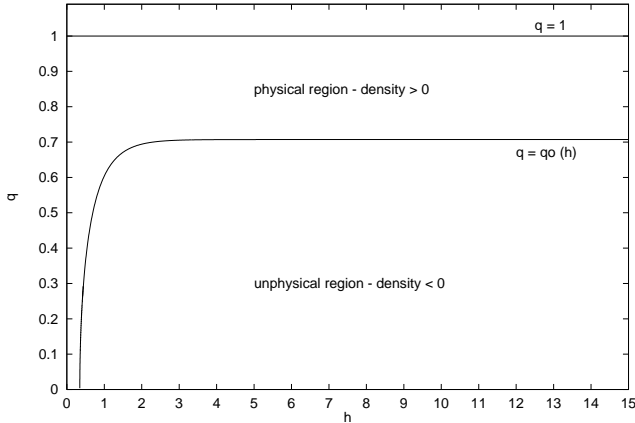


Fig. 13. Parameter space (h, q) of the logarithmic Hamiltonian (17). The physical region is determined by $q_0(h) \leq q \leq 1$ where $q_0^2(h) = 0.5 - e^{-2h}$ (see Sect. 2.2 and text)

leading to an enlargement of the layer and therefore to a larger domain of irregular motion. A few small and not too small islands are embedded in this chaotic zone, some of them are indicated in both figures. All the thin peaks observed in both figures correspond to hyperbolic orbits. Therefore we obtain a picture of the hyperbolic structure of the phase space that announces the future appearance of irregular motion as soon as we increase the perturbation (to be precise, irregular motion certainly exists around all these resonances but it is confined to a set of negligible measure). Additionally σ_{1s} reveals some details about the internal structure of the secondary resonances.

5. Global dynamical properties

5.1. Parameter space and stability of main periodic orbits

Let us now investigate the global dynamical properties of the logarithmic potential in the parameter space (h, q) . In what follows we use the formulation given in Sect. 3, denoting the dimensionless energy and time again by h and t , and the variables as lowercase. To get the “true” energy (i.e., in the old variables) just compute $p_0^2(h + \ln r_c)$ with $p_0^2 = 2$ and $r_c = 0.1$ (see Eq. (17) and discussion around).

First we consider the parameter space. In Sect. 2.2 we show that q should be restricted to some domain, $q_0(h) \leq q \leq 1$, to have the logarithmic model physical sense; $q_0^2(h) = 0.5 - \exp(-2h)$. This subspace defines in the hq -plane the “physical region” where the density is positive everywhere. This is sketched in Fig. 13 where we see that for $h \gtrsim 2$, the physical region is restricted to $\sqrt{2}/2 \lesssim q \leq 1$. For $h \leq \ln 2/2$ no bounds for q exist. Therefore to explore the dynamics for generic values of the energy ($h \gtrsim 2$), $q_0^* = 0.71$ is a good lower bound for q .

Next we discuss the stability of the long-axis and short-axis periodic orbits. The stability analysis is done by

means of a standard Floquet technique and using the fact that both orbits are periodic orbits of 1D Hamiltonians with period T_x and T_y , respectively. Let us summarise the procedure.

From (17) and denoting, as before, by $\phi(x, y)$ the potential, for the long-axis periodic orbit, we have

$$\dot{p}_x = -\phi_x(x, 0) = -\frac{x}{x^2 + 1}, \quad \dot{x} = p_x. \quad (27)$$

Let $\varphi_x(t)$ be a T_x -periodic solution for $x(t)$. Consider now the normal variational equations to the latter vector field for $\varphi_x(t)$, that is,

$$\delta \dot{p}_y = -\phi_{yy}(\varphi_x(t), 0)\delta y = -\frac{1/q^2}{1 + \varphi_x^2(t)}\delta y, \quad \delta \dot{y} = \delta p_y. \quad (28)$$

In a similar way, for the short-axis periodic orbit, we obtain

$$\dot{p}_y = -\frac{y/q^2}{y^2/q^2 + 1}, \quad \dot{y} = p_y,$$

which, after scaling to $z = y/q$, $p_z = qp_y$ and $s = t/q$, can be written as

$$p'_z = -q\frac{z}{z^2 + 1}, \quad z' = \frac{p_z}{q}, \quad (29)$$

where prime means derivative respect to s . Denote with $\varphi_z(s)$ a S_y -periodic solution for $z(s)$ ($S_y = T_y/q$). The normal variational equations are then

$$\delta p'_x = -\frac{q}{1 + \varphi_z^2(s)}\delta x, \quad \delta x' = q\delta p_x. \quad (30)$$

The equations of motion (27), (29), and the variational ones (28), (30), can be reduced to a single pair of coupled differential equations of the form

$$\frac{d^2 w}{d\tau^2} + \frac{w}{1 + w^2} = 0, \quad \frac{d^2 \xi}{d\tau^2} + \frac{\beta}{1 + w^2}\xi = 0, \quad (31)$$

where, for the x -axis orbit, $\tau = t$ and $\beta = 1/q^2$ while, for the y -axis orbit, $\tau = s = t/q$ and $\beta = q^2$. Therefore, the stability of both orbits can be studied in the $h\beta$ -plane. The region defined by $q_0^2 < \beta < 1$ corresponds to the y -axis orbit while that where $1 < \beta < 1/q_0^2$ to the x -axis orbit.

The first in (31) leads to

$$\frac{1}{2} \left(\frac{dw}{d\tau} \right)^2 + \frac{1}{2} \ln(1 + w^2) = h. \quad (32)$$

From the latter, it is possible to derive asymptotic expressions for the period, $P(h)$, of any orbit at a given h level. Indeed, after change of variables, it is easy to show that

$$P(h) = 4e^h I(h), \quad I(h) = \int_0^{\sqrt{2h}} \frac{e^{-x^2} dx}{\sqrt{e^{-x^2} - e^{-2h}}},$$

which for small and large energies reduces to

$$P(h) \approx 2\pi(1 - h)e^h \quad h \ll 1,$$

$$P(h) \approx 2\sqrt{2\pi}e^h \quad h \gg 1.$$

Here $P = T_x, T_y/\sqrt{\beta}$ for the x - and y -axis orbit, respectively. So, in terms of the original variables like in (16), $h \rightarrow h/p_0^2 - \ln r_c$, $t \rightarrow p_0 t/r_c$ and for $h \gg p_0^2 \ln r_c$ we get

$$T_x(h) \approx \frac{2\sqrt{2\pi}}{p_0} e^{h/p_0^2}, \quad T_y(h) \approx qT_x(h). \quad (33)$$

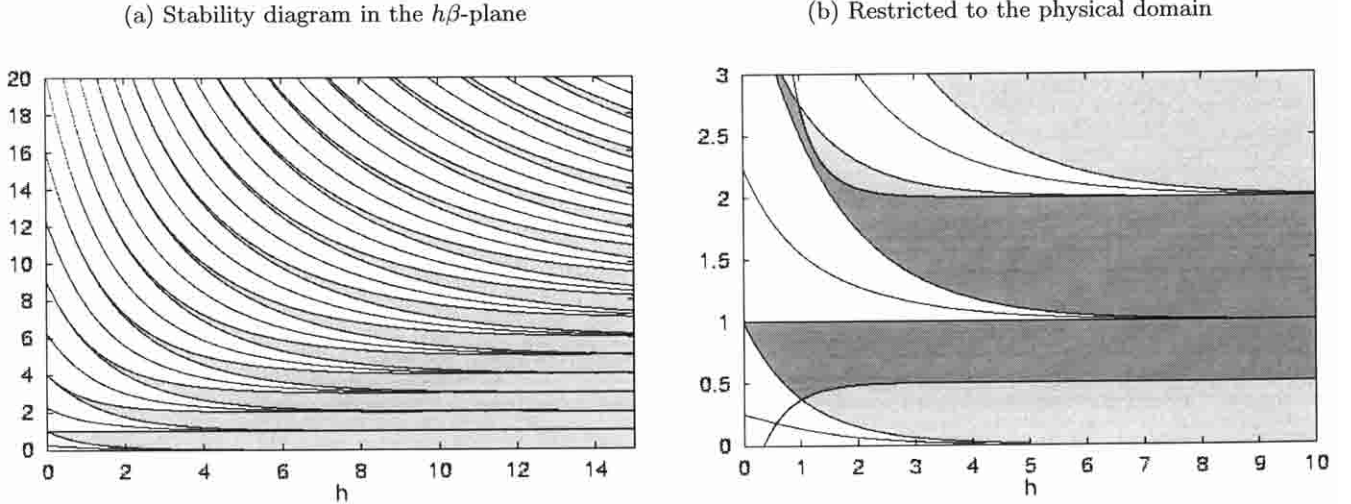


Fig. 14. **a)** Stability of the long and short-axis periodic orbits. Horizontal axis: dimensionless energy, h ; vertical axis: β . For the short-axis orbit, $\beta = q^2 < 1$, while $\beta = 1/q^2 > 1$ corresponds to the long-axis orbit. Grey: instability regions, $\text{Tr}(M) > 2$; white: stability regions, $\text{Tr}(M) < 2$; lines: $|\text{Tr}(M)| = 2$. **b)** The same but restricted to the physical domain defined by the curves $q_0^2(h) \leq \beta \leq 1/q_0^2(h)$. Dark grey: instability “r” regions inside the physical domain. See text for details

In a similar way we have $T_x(h)$ and $T_y(h)$ for small h .

The stability index is defined, as usual, by the trace of the monodromy matrix associated to (31). That is, defining $\eta = d\xi/d\tau$ and $\xi = (\xi, \eta)$, the second in (31) can be written as $d\xi/d\tau = D(w; \beta)\xi$ where D is the 2×2 differential matrix $D_{11} = D_{22} = 0$, $D_{12} = 1$, $D_{21} = -\beta/(1+w^2)$. Thus if we write $\xi(\tau) = A(\tau)\xi_0$, being ξ_0 any initial condition and $A(0) = \text{Id}$, then $A(\tau)$ satisfies the equation,

$$\frac{dA}{d\tau} = D(\varphi_w(\tau); \beta)A \quad (34)$$

where $\varphi_w(\tau)$ is a $P(h)$ -periodic solution of the first in (31) or of (32). The monodromy matrix is, by definition, $M = A(P(h))$. To compute M we have to solve (34). However, as the flow is invariant by the change $(\xi, \eta, t) \rightarrow (\xi, -\eta, -t)$, then one has $A_{11} = A_{22}$, using the symplectic character of $A(\tau)$. So to get $\text{Tr}(M)$ it is enough to solve for the first column of A . A periodic orbit is linearly stable (unstable) if $|\text{Tr}(M)| < 2$ (> 2). In case $|\text{Tr}(M)| = 2$, the orbit is said to be marginal stable. For these particular periodic orbits of the logarithmic potential, one has immediately that $\text{Tr}(M) \geq -2$. So, instability comes only from $\text{Tr}(M) > 2$. This is due to the fact that $D(\varphi_w(\tau))$ is $P/2$ -periodic, so $M = A(P/2)^2$ and as $A(P/2)$ is real symplectic, M cannot have negative eigenvalues.

In Fig. 14a we present the stability diagram of both periodic orbits for $0 \leq h \leq 15$ (i.e., a true energy interval about $[-4.6, 25.4]$) and $0 \leq \beta \leq 20$. The region defined by $\beta = q^2 < 1$ corresponds to the stability diagram of the y -axis orbit while that for $\beta = 1/q^2 > 1$ to the x -axis orbit. We plot in grey those zones where $\text{Tr}(M) > 2$, in white those where $\text{Tr}(M) < 2$ and the lines are level curves of $|\text{Tr}(M)| = 2$. From $(h, \beta) = (0, n^2)$ ($n \neq 0$ integer) emanate the so-called instability tongues. This behaviour is due to the parametric resonance. Indeed, the second

in (31) for small h can be written as $\ddot{\xi} + [\beta + \mu(h)c(t)]\xi = 0$ where $c(t)$ is periodic and $\mu(0) = 0$. For general P -periodic $c(t)$, for instance, $c(t) = \cos(2\pi t/P)$, the instability tongues would emanate from $(\mu, \beta) = (0, n^2/4)$. This is the well known result for the classical Mathieu equation (see, for example, Broer & Levi 1995 and references therein as well as Broer & Simó 1998 for the related unfoldings). However, in our case, the instability tongues emanating from $(0, (2k+1)^2/4)$ do not show up and only appear at $(0, n^2)$.

It is also worth to mention that the boundaries of the instability zones ($\text{Tr}(M) = 2$ in the present case) correspond to values of β for which the second equation in (31) has a periodic solution with the same period of the first in (31). This periodic solution performs n full oscillations (i.e., it has exactly $2n$ changes of sign) for any point on the boundary of the n -instability tongue, counted from the bottom. The differences between the two boundaries are as follows: assume that the first in (31) is started, at $\tau = 0$ with $w = 0$ and $dw/d\tau > 0$. Then, for the lower boundary, the periodic solution of the variational equation is the first column of the matrix A , the upper boundary is the second column. In an equivalent way, the monodromy matrix, M , has in both cases 1 at the diagonal, and for the lower boundary, $M_{21} = 0$, $M_{12} \neq 0$, while $M_{21} \neq 0$, $M_{12} = 0$ for the upper one.

As long as h increases, the unstable zones become wider. Note that the width of these zones approaches asymptotically to a fixed value, $\Delta\beta_n = 1$ (see Appendix for a proof of this claim). This is more evident for $0 \leq \beta \lesssim 8$, where the stability regions are extremely narrow at high energies. The convergence of $\Delta\beta_n \rightarrow 1$ is the faster the smaller is n . For larger values of β , $\beta \gtrsim 8$, the stability zones (for the x -axis orbit) become significant.

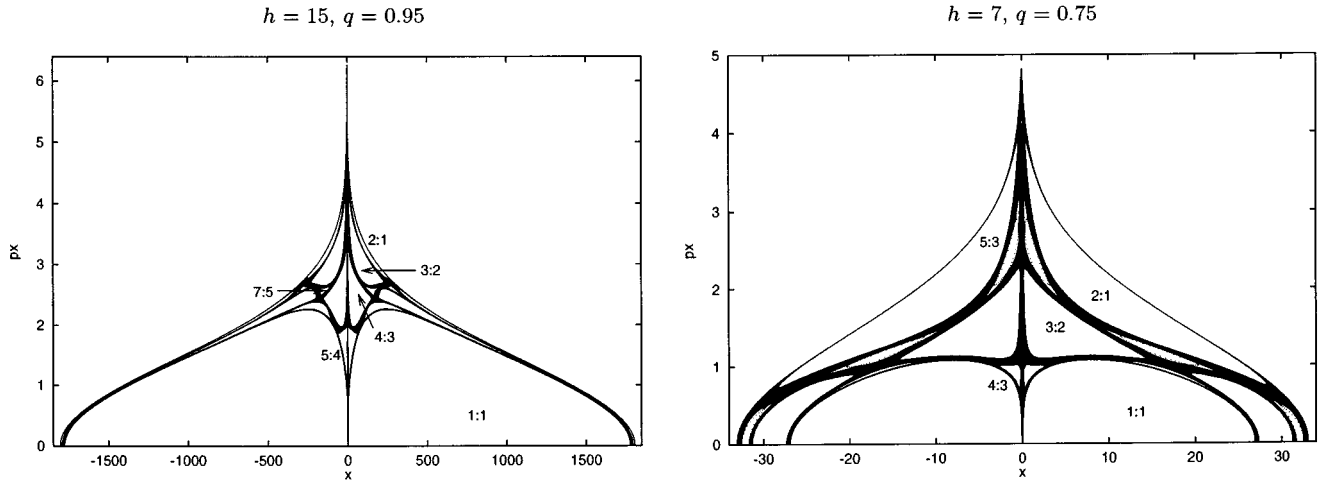


Fig. 15. Surface of section (x, p_x) , for $h = 15$ and 7 (about 9.8 and 5.8 in dimensionless units) with $q = 0.95$ and 0.75 and $r_c = 0.1$, $p_0^2 = 2$, corresponding to the principal resonances $(\omega_y/\omega_x = a:b)$ and their associated stochastic layers (see text)

Nevertheless almost all of them lie in the unphysical domain. In Fig. 14b we restrict the parameter space to the physical domain, $q_0^2(h) \leq \beta \leq 1/q_0^2(h)$, where we see that for large h ($h \gtrsim 4$), the region is bounded by $0.5 \lesssim \beta \lesssim 2$ while for small h ($h \leq \ln 2/2 \approx 0.35$), $0 < \beta < \infty$. In this figure we plot in dark grey the unstable zones inside the physical region. We observe that the y -axis periodic orbit ($\beta < 1$) is always unstable except in some zone of the “harmonic oscillator regime” ($h \ll 1$). In this regime and for $h \lesssim 0.3$ the y -axis orbit is unstable if $q (= \sqrt{\beta})$ is close to 1, due to the parametric resonance. On the other hand, the x -axis orbit ($\beta > 1$) appears to be always stable in the low energy regime. Only a very narrow zone of instability is present, for $h \lesssim 1$ and $\beta \gtrsim 2.5$ ($q \lesssim 0.63$). In the range $1 \lesssim h \lesssim 7$, the x -axis orbit can be either stable or unstable. The stability zone becomes very narrow when we approach $h \approx 7$; β is confined to a small interval of the form $(1, 1 + \varepsilon(h))$, where $\varepsilon \rightarrow 0$ as $\delta \exp(-\gamma h)$, γ close to 1 and, for instance, $\varepsilon \approx 0.089, 23.5 \cdot 10^{-6}, 23.8 \cdot 10^{-10}$ for $h = 5, 15, 25$, respectively. For large energies, $h \gtrsim 7$, the x -axis orbit is unstable except for q extremely close to 1. Note that for $4 \lesssim h \lesssim 7$, this orbit is stable in two different β intervals, one is that mentioned above and, the second one, starts just beyond the physical region, at $\beta \approx 2$ ($q \approx \sqrt{2}/2$). The latter result confirms the conjecture given by MS89 about the border of this second stability domain.

To complete this section let us say a few words about the 1:1 periodic orbit. As we have already mentioned in Sect. 2, this orbit is always stable for any physical value of q . Using the formulation given in that section, the rotation period for this orbit can be approximated by

$$T_{1:1}(h) = \frac{2\pi}{\omega_\theta} \approx \frac{2\pi}{p_0} \exp(-(1 + \alpha/2)/2) e^{h/p_0^2}, \quad (35)$$

where $\alpha = (1 - q^2)/q^2$. This estimation is obtained using the fact that if α is not too large, the 1:1 orbit is nearly

circular and then $T_{1:1} \approx 2\pi a/v_c$, where a is the circular radius given by (12) and v_c , the circular speed, is approximately p_0 . From (33) and (35) for $h \gg p_0^2 \ln r_c$, we obtain

$$\frac{T_{1:1}}{T_x} \approx \sqrt{\frac{\pi}{2e}} e^{-\alpha/4} \approx 0.76 e^{-\alpha/4},$$

independent of h . This estimation of the periods agrees, roughly, with the accurate values given by PL96 for relatively small h (-0.4059).

5.2. Irregular motion

In this section we investigate some aspects of the stochastic component of the phase space associated to the logarithmic potential. In Sect. 4.2 we showed, for three values of q (0.9, 0.8, 0.7) and for only one of the energy (-0.4059), that the motion in the logarithmic potential is mostly regular but populated by many resonances. The stochastic component appears to be confined to the gross stochastic layer where the short-axis orbit lies and, in some cases, to the thin layer corresponding to the long-axis orbit. Within the box domain some other chaotic regions are present, for instance, around the 4-periodic island chain that appears close to the gross stochastic layer (see Fig. 9 for $q = 0.7$ and below). To sketch this, in Fig. 15 we show surfaces of section (x, p_x) for comparatively large values of the energy, $h = 15, 7$ and two extreme cases $q = 0.95, 0.75$. In any of these figures we recognize the main resonances, given by ω_y/ω_x , that lead to loop (1:1), pretzel (4:3), fish (3:2), banana (2:1) and other high order resonances (5:4, 7:5, 5:3, for instance) – see MS89 for the terminology on the periodic orbits and several illustrations. All of them are surrounded by a stochastic layer where the associated unstable periodic orbits lie. It seems that, for these particular values of h and q , all the layers are connected in a single stochastic channel. For comparatively large energies, box

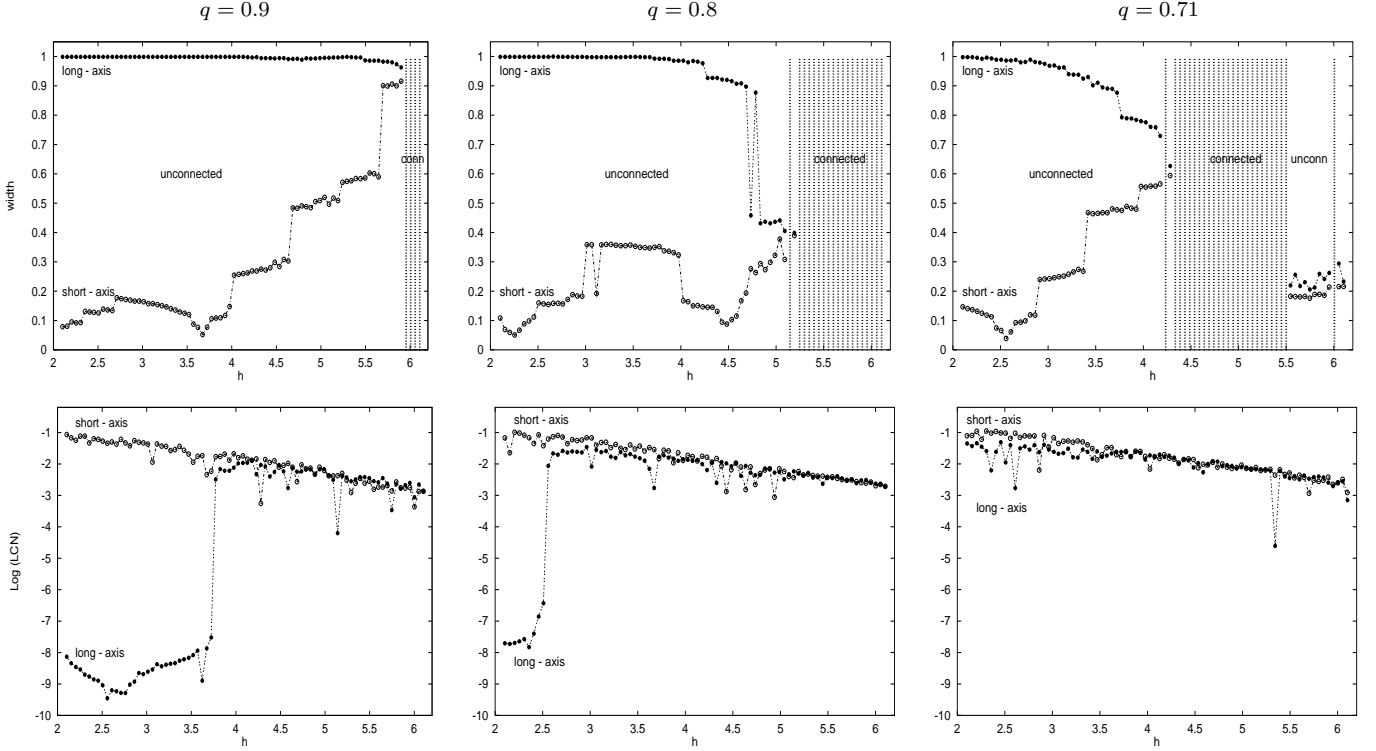


Fig. 16. (Top) Width of the stochastic layers where the short and long-axis orbits lie against the dimensionless energy, h , and for three representative values of q . (Bottom) $\text{Log } \sigma$ after $T(h) \approx 10^4 T_x(h)$ for both layers. See text for details

orbits disappear leading to boxlets. Certainly, within the loop domain, some isolated chaotic zones should exist.

An interesting aspect to investigate is the connection between different stochastic regions. The results given in Sect. 4.2 for $h \approx -0.4$ and $q = 0.7$, show that the stochastic layer around the 1:1 resonance is not connected with that of the 4:3. The same happens with the layers surrounding the 4:3 and 3:2, 3:2 and 5:3, 5:3 and 2:1 resonances. It is clear that the overlap would occur at higher energies. A formal way to investigate connections between different resonances (heteroclinic connections) would be to follow the evolution of any initial condition taken along the unstable manifold associated to each resonance. However, in this case this approach is not so simple. The periodic points associated to, for instance, the 4:3 and the 3:2 resonances change their location and stability properties as h varies. For example, in Fig. 15 the most relevant hyperbolic points lie on the p_x axis, but for lower energies, some of them appear as elliptic on this axis. So, to locate the unstable manifolds, we should look for the hyperbolic points somewhere out of the p_x axis. While this is not a serious complication we have taken a simpler approach.

Therefore we consider the connection between the stochastic layers surrounding the 1:1 and 2:1 resonances. That is, we deal with the problem of finding h such that a point close to the origin at $t = 0$ is close to the border of the section at $t = T$. So, the derived critical

energy, $h_c(q)$, is an upper bound to connections with other stochastic layers between them. We study the energy range $[-0.4, 7.6]$, about $[2.1, 6.1]$ in dimensionless units, with step 0.1 and three representative values of q , 0.9, 0.8 and 0.71. For each energy level we take two orbits such that, at $t = 0$ one is close to $(x, p_x) = (0, 0)$ and the other close to $(0, p_x^*(h))$, where $p_x^*(h) = (2h - p_0^2 \ln r_c^2)^{1/2}$. Typically we take $(0, \epsilon)$ and $(0, (1 - \epsilon)p_x^*(h))$ with $\epsilon = 10^{-7}$. The reason to take ϵ so small is due to the structure of the stochastic layer (if it exists, that is, if the orbit is unstable). The external part of the layer, close to the border, is populated by many small resonances. If the initial condition falls inside any of them, the orbit will be confined there forever. On the other hand the central part of the layer, around the separatrix, looks like ergodic and therefore it appears to be appropriate to take the initial condition in this part (for details, see Chirikov 1979, Sect. 6).

Next, using the transformation given in Sect. 3, we pass to the variables (x_1, x_3) defined in (20). In this way $0 \leq |x_3| \leq 1$. Each point is followed during $3.5 \cdot 10^4$ consequents on the Poincaré section $y = x_2 = 0$. During the computation we restrict the attention to a small x_1 interval centered at the origin, typically, $|x_1| \leq 0.05$. Within this interval we look for the maximum distance between $(x_1(t), x_3(t)) \approx (0, x_3(t))$ and the points $(0, 0)$ and $(0, 1)$. Then we define the width of the layer as $W_s = \max\{|x_3|\}$; $W_1 = \min\{|x_3|\}$ depending whether we start from the

neighbourhood of the short-axis or long-axis orbit, respectively. The results are presented in Fig. 16 where we include the computed LCN, σ , (actually, σ_{1s} using the MEGNO) for the same orbits and for a motion time, $T(h) = 10^4 T_x(h)$, with $T_x(h)$ given by (33).

The criterion to determine $h_c(q)$, for which the layers are connected, is $W_s(h_c) \geq W_1(h_c)$. But W depends also on time: W_s (resp. W_1) would increase (resp. decrease) with T . The results shown in Fig. 16 are for a given motion time, $T \approx 3 \cdot 10^4 T_x$, which appears to be large enough for our purpose. A dependence with respect to the initial conditions has to be expected too. Take, for instance, the plot for $q = 0.9$. The layers are clearly connected at very high energies, beyond $h \approx 6$. The layer around the 1:1 resonance increases its width discontinuously except in some energy interval, $2.7 \lesssim h \lesssim 3.7$, where it decreases. This may be due, perhaps, to the appearance of the 4:3 elliptic point on the p_x axis. The abrupt change in the width observed at $h \approx 4, 4.6, 5.5$ could be attributed to connections with the layers of the 4:3, 3:2 and 5:3 resonances, respectively. The LCN for the 1:1 stochastic layer decreases monotonically with h without major deviations. This reduction of the LCN with h is due to the exponential dependence of the period with h (see below).

The x -axis orbits look stable for small h , as the LCN indicate. For $h \gtrsim 3.5$ it turns unstable but the stochastic layer is rather thin, W_1 is very close to 1 for $h \lesssim 5$. The values of the LCN suggest that the layers could be connected at $h \approx 5.5$ while W_s reaches W_1 at $h \approx 6$. Along the range $5.5 \lesssim h \lesssim 6$, W_s and W_1 are close one another. Therefore the critical value $h_c(0.9)$ lies somewhere between (5.6, 5.9).

A similar picture is observed for $q = 0.8$ and 0.71 , but the overlap of the layers takes place for smaller h as q decreases. A simple inspection of the figures suggests that $h_c(0.8) \approx 5$ and $h_c(0.71) \approx 4$. In the last case ($q = 0.71$) we observe a zone beyond h_c , $5.5 \lesssim h \lesssim 6$, where the layers appear unconnected. It may occur that some KAM curve actually exists, acting as a barrier to the diffusion or, perhaps, that a larger motion time would be necessary. In this direction, a few surfaces of section performed for these values of h and q , but for much larger motion times, do not provide any definitive answer. Anyway, in this interval, W_s and W_1 are very similar. The main difference between the three figures is that, while for $q = 0.9$ W_s reaches values close to 0.9, for $q = 0.8$ and 0.71 W_s does not exceed 0.6.

An interesting point is that $\log \sigma$ for the gross stochastic layer decreases linearly with h . We fit by least squares the function

$$\log \sigma(h, q) = c(q)h + d(q), \quad (36)$$

obtaining $c(0.9) \approx -0.457$, $c(0.8) \approx -0.438$, $c(0.71) \approx -0.421$; $d(0.9) \approx -0.09$, $d(0.8) \approx -0.08$, $d(0.71) \approx -0.06$. These estimations reveal that the LCN for the layer does not depend strongly on q , being the latter number sensitive to just one parameter, h . Nevertheless, in (36) we do

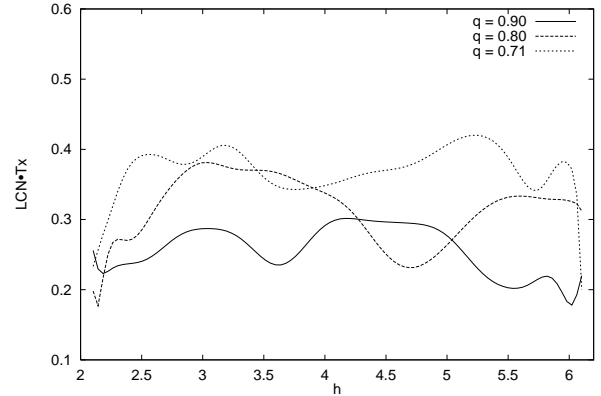


Fig. 17. Dependence of $\sigma(h, q)T_x(h)$ on h for the 1:1 stochastic layer and three different values of q . For the computation we use the values of the LCN presented in Fig. 16 and T_x given by (33). See text

not take into account the dependence of T_x on h . That is, $T_x(h)$ was considered above only to make the computation of the LCN over similar time-scales for different energy surfaces. Therefore to obtain a meaningful result we should calculate $\sigma(h, q)T_x(h)$. Assuming that the values -0.44 , -0.08 are representative for $c(q)$ and $d(q)$, respectively, then using (33) for $T_x(h)$ and scaling in (36) $h \rightarrow h/p_0^2 - \ln r_c$ with $p_0^2 = 2$ and $r_c = 0.1$, it is straightforward to get

$$\sigma(h, q)T_x(h) \approx 0.3,$$

independent of h . Thus, for any energy level, $T_L(h) \approx 3 T_x(h)$, which is consistent with the values obtained in Sect. 4.2. This result is shown in Fig. 17 where we observe that σT_x is nearly constant, the smaller is q the larger is σT_x . In any case, the LCN is bounded by $0.2 \lesssim \sigma T_x \lesssim 0.4$.

The results presented in this section suggest that the motion in the logarithmic potential is mainly regular. As the energy increases, irregular motion appears confined to comparatively narrow stochastic layers. Connections among them occur at moderate-to-large energies and through thin filaments. An interesting fact is that the Lyapunov time, for the main stochastic zone, is rather short and almost independent of h and q . Note that, a similar calculation to that performed in Fig. 9 but for $h \gtrsim h_c$ would lead, for “boxes”, to a completely chaotic scenario. But this is due to the choice of the one dimensional initial condition space on the xp_x -plane (the p_x axis). As mentioned in Sect. 4.2, initial conditions taken along a maximum circle on the 2D sphere (see Fig. 6) would provide a more realistic picture.

Another point that should be mentioned is that for large energies, say $h \gtrsim h_c$, the dynamics becomes almost independent of h , being q the relevant parameter. In this direction, Fig. 15 is representative of the general structure of the phase space associated to the logarithmic potential

at different q levels. In fact, as h increases, the potential model approaches to the singular logarithmic potential, where the relevant parameter is only q (see Appendix).

6. Discussion

In this work we have shown that detailed information about global and local dynamics can be obtained by means of simple tools. In the first part we take advantage of the pendulum model and its corresponding Hamiltonian (the pseudo-invariant \mathcal{K}) to derive the basic dynamics of a general bar-like system. The numerical evidence shows that even if the potential is comparatively far from the central symmetry, the tangential motion (at moderate-large radii) is well represented by a pendulum. Therefore we can use all the theory behind this universal system to explain loop and box orbits, the stochastic layer and how this picture changes as the perturbation increases. However to get more insight about the structure of the phase space we need the help of another technique.

In Sect. 1 we said that alternative tools were proposed to explore the phase space. Let us summarise then the most often used in Galactic Dynamics by means of a comparative discussion with the MEGNO;

a) The computation of the Poincaré surface of section is the most popular technique to sketch the basic dynamics. However it works in a simple way in 2D systems and, to obtain details about the fine structure of the phase space, one needs very long integrations. This is evident from Fig. 11a where we needed a comparatively large computational effort to obtain the first details of the resonance structure close to the stochastic layer. In fact, many small resonances marked in the corresponding figure for σ_{1s} (Fig. 10) are not visible in this high resolution surface of section.

Besides a 2D plane is not, in general, the natural space to display the motion. Figure 6 shows that, at least for the potential considered here, the 2D sphere is the natural manifold to represent the dynamics.

For higher dimensional problems one can use a combination of Poincaré maps with a slicing technique (see, for instance, Simó et al. 1995 for some examples). But a systematic use of this approach requires more computational and graphic effort;

b) As we have already said, the computation of the LCN is widely used to separate regular and different chaotic components of the phase space (each of them, in general, with different Lyapunov times). The works of Udry & Pfenniger (1988), Merritt & Friedman (1996) and Wozniak & Pfenniger (1999) are a few examples of applications to models of triaxial elliptical and barred disc galaxies. However, as we showed above, the classical LCN technique is not useful to investigate the fine structure of the regular component. Moreover, to separate regular and irregular regions with $T_L \gtrsim 10^3$ periods, the motion time should be very large, $T \sim 10^4 - 10^5$ periods at least;

c) The spectral analysis introduced by Binney & Spergel (1982, 1984), is basically a Fourier analysis of the orbit. Recently, Carpintero & Aguilar (1998) developed an efficient algorithm, following the approach of Binney & Spergel, that provides information about the frequencies associated to the invariant torus where the motion proceeds (see however item d). The latter algorithm is able to classify orbits in different families and to distinguish the presence of irregular, stochastic motion in relatively short motion times, less than 10^3 periods;

d) The most powerful tool at hand is, perhaps, the FMA due to Laskar (1990, 1993, 1999) and applied to Galactic Dynamics by, for instance, PL96, Wachlin & Ferraz-Mello (1998), Papaphilippou & Laskar (1998), Valluri & Merritt (1998). This technique, specifically proposed to the study of dynamics in the Solar System is, in fact, similar to the spectral analysis but developed in a much more sophisticated way. In general, the FMA provides, for short-to-moderate motion times ($\lesssim 10^3$ periods, depending on the needed accuracy), very precise estimates of the frequencies (if they exist, that is if the motion takes place on a torus) and hence information about the global dynamics, details concerning the fine structure of the phase space (high-order resonances) and a relatively clear identification of the chaotic regions (where the precise determination fails). See also Gómez et al. (1987) for an alternative approach with applications to Space Science.

Even though with this tool it is possible to derive a diffusion-like coefficient in frequency space, its connection with the LCN has not been established yet. In fact it is unclear that the mean-rate of variation of frequencies over a given time interval, that is the lack of precise estimates of the frequencies, provides direct quantitative information about the “amount of hyperbolicity”, being the latter measured by the LCN. Papaphilippou & Laskar (1998), Valluri & Merritt (1998) associate the diffusion rate of a given orbit in a 3D Hamiltonian with the maximum mean-rate between both rotation numbers, ω_x/ω_z , ω_y/ω_z . But from standard theory of diffusion, it seems that the diffusion coefficient should be related with the mean square value instead with the mean value. This is the way in which, for instance, Chirikov defines the diffusion rate to investigate diffusion in phase space (including Arnold diffusion, see Chirikov 1979 Sects. 5.4, 7.2 and 7.3). A different approach (but with the same result) is given by Saslaw (1985)–Ch. 4, where he illustrates the diffusion process in phase space by means of the one dimensional Fokker-Planck equation.

The FMA is developed in the framework of near-integrable Hamiltonian systems. For these systems, with the phase space almost entirely foliated by invariant tori, this technique proves to be very useful. As shown in Figs. 10 and 12, σ_{1s} as well as \mathcal{J} (Fig. 11b) reveal much more details about the resonance structure than the FMA. Only a few of the resonances marked in those figures are

present in Figs. 8 and 9 of PL96 (at least for the graphical resolution of their figures). In that figures PL96 plot the rotation number, r , defined as ω_x/ω_y for boxes and ω_θ/ω_r for loops, against the parameter that label each family, p_{x_0} and x_0 respectively, for $q = 0.9, 0.8$ and 0.7 . In all cases we observe a regular, monotonous dependence of r on p_{x_0} and x_0 except in some regions where the curve is not regular. Scattered points mean irregular orbits, an horizontal plateau a stability island and a small gap an unstable periodic orbit. The value of r in those zones where it is constant or undefined provides the order of the resonance and the width of the plateau or the gap, a measure of the resonance size.

In this direction, the MEGNO is able to give the actual size of a resonance as well as to put in evidence its internal structure. Besides we get simultaneously a good estimate of the LCN with a comparatively small computational effort. Both σ_{1s} and $\bar{\mathcal{J}}$ reveal the hyperbolic structure of the phase space. This tells us where irregular motion would appear when the perturbation is enlarged or when additional degrees of freedom are added. This last point will be investigated by means of the MEGNO in a separate paper.

The FMA gives an accurate value of the rotation number, a label for each resonance. So, it is possible to follow the evolution of a given resonance as the perturbation changes while, for instance, from Fig. 12 it is not evident how to do that when we change the value of q , unless a systematic continuation of periodic orbits vs. q is done. Hence the combination of the MEGNO with a precise spectral analysis would lead to a complete description of the dynamics;

e) The spectra of stretching numbers, helicity and twist angles proposed by Contopoulos & Voglis (1996, 1997). An application to a 2D model of barred galaxy is given by Patsis et al. (1997). The main advantage of this tool is its efficiency to separate regular and stochastic domains in rather short motion times, $\lesssim 50$ periods;

f) In two recent papers, Cincotta & Simó (1999, 2000) proposed the conditional entropy of nearby orbits, I , defined through the arc length parameter along the orbit instead of the time as a random variable, as an efficient tool to investigate the phase space as well as to derive the LCN in realistic physical times ($\sim 10^3$ periods). In fact, the indicator \mathcal{J} was defined here in such a way that it behaves in a similar manner than the logarithmic time-derivative of I , $J = d \log I / d \log T$. The main difference between J and \mathcal{J} is that the former is a second order magnitude in δ (at first order $J \equiv 0$) while, by definition, \mathcal{J} is linear in δ . Hence, J appears to be rather sensitive to the presence of periodic orbits and, when the region of the phase space under study includes several high order resonances, J looks noisy and depends more strongly on the time step. For instance, in Cincotta & Simó (2000) we study several orbits in the window shown in Fig. 11a by means of the conditional entropy and even though the resonance structure

is visualized, the picture is not as clear as that provided by \mathcal{J} . This can be understood recalling that in this small interval 43 periodic orbits with period ≤ 50 exist. However the first applications of the conditional entropy to simple potentials (Hénon & Heiles 1964, for instance) show that it is also a powerful tool. Some analytical arguments behind this method are given in the mentioned papers but a rigorous theory is still lacking.

In conclusion we can say that the MEGNO resumes almost all the nice features of the methods mentioned above. In fact, it is effective to obtain relevant information about global dynamics and the fine structure of the phase space with a relatively small computational effort. The indicator \mathcal{J} allows to identify clearly regular and irregular motion as well as stable and unstable periodic orbits. A linear least squares fit of $\bar{\mathcal{J}}(T)$ is enough to get a good estimate of the Lyapunov time in regular and irregular components of the phase space. Indeed, the MEGNO is the simplest way to obtain such information on the phase space, since it has been tailored taking advantage of our knowledge on the basic dynamics in this kind of systems. The derivation of the LCN from the MEGNO rests on the idea that much information about the dynamics is contained in the time evolution of an single orbit $\gamma(t)$ and in the tangent vector $\delta(\gamma(t))$ and the least squares fit is a first attempt to extract this information. These questions, as well as the use of a single orbit (instead of an ensemble) to investigate the structure of one component or the irregular part of the phase space will be the subject of a future paper.

Finally, in what respects to the 2D logarithmic potential, we can say that the results given in this work together with the studies performed, for instance, by MS89 and PL96 resume almost all the dynamics of the model.

Acknowledgements. The first author would like to acknowledge the hospitality of the Departament de Matemàtica Aplicada i Anàlisi, Universitat de Barcelona where this work was done and the Consejo Nacional de Investigaciones Científicas y Técnicas de la República Argentina who supported his visit to the University of Barcelona. The second author has been supported by DGICYT grant PB 94-0215 (Spain). Partial support from the catalan grant CIRIT 1998S0GR-00042 is also acknowledged. Both authors are grateful to an anonymous referee for a careful reading of the manuscript and helpful recommendations.

Appendix: Some mathematical results

Here we collect some mathematical results concerning the logarithmic potential and mainly related to the limit case $r_c \rightarrow 0$ for a fixed value of h or, equivalently, $h \rightarrow \infty$ for a fixed value of r_c .

First we consider the collinear problem $\ddot{x} = -x^{-1}$. For other similar problems but with different exponent, for instance, $\ddot{x} = -x^{-\gamma}$, $\gamma \neq 1$, and with Hamiltonian $H = y^2/2 + x^{1-\gamma}/(1-\gamma)$, the scalings $x = \alpha z$, $t = \beta s$

lead to ($' \equiv d/ds$) $\alpha\beta^{-2}z'' = -\alpha^{-\gamma}z^{-\gamma}$, which has the same form as before if $\beta^2 = \alpha^{\gamma+1}$. Let $w = z'$ and $\hat{H} = w^2/2 + z^{1-\gamma}/(1-\gamma)$. Then the level of energy, $H = h$ and $\hat{H} = \hat{h}$ are related by $\hat{h} = h\alpha^{\gamma-1}$. Hence, \hat{h} can be scaled to the values 1, 0 or -1 . Furthermore, a collision solution (i.e. of unbounded acceleration) leaving from (or ending at) $x = 0$ for $t = 0$ is of the form $x(t) = at^b + \dots$ with $b = 2(1+\gamma)^{-1}$, $a = ((1+\gamma)^2/2(\gamma-1))^{1/(1+\gamma)}$, if $\gamma > 1$. For $\gamma = 1$ and $H = y^2/2 + 0.5 \ln x^2$, the scalings defined above lead to $\alpha = \beta$ and $h = \hat{h} + \ln \alpha$. So we can always reduce to the level $\hat{h} = 0$ setting $\alpha = e^h$ and then $|x| \leq 1$.

To solve the equations of motion $\dot{x} = y$, $\dot{y} = -x^{-1}$ with $|x| = e^{-y^2/2}$, it is convenient to use y as independent variable. Then, for $x > 0$, and assuming that at $t = 0$, $y = +\infty$, $x = \sqrt{2\pi}N(y)$, $t = \sqrt{2\pi}F(-y)$, where N , F ($F \equiv \int_{-\infty}^y N(u)du$) denote, respectively, the density and distribution function of the standard normal law (0 average and standard deviation 1). In particular, a solution leaving from collision ends again at it ($y = -\infty$) after $t = \sqrt{2\pi}$. Furthermore, as

$$F(y) = \frac{e^{-y^2/2}}{\sqrt{2\pi}} \frac{1}{|y|} \sum_{n \geq 0} \frac{(-1)^n (2n-1)!!}{y^{2n}} \quad (37)$$

is the asymptotic series for $y \rightarrow -\infty$ (with error less, in absolute value, than the first neglected term), the relation $x(t) = t\sqrt{\ln t^{-2}} (1 + \mathcal{O}(\ln(\ln t^{-1})/\ln t^{-1}))$ for $t \rightarrow 0$ follows immediately. Due to the symmetry, the same relation applies when $y \rightarrow -\infty$ but $t \rightarrow \sqrt{2\pi} - t$. Note that y decreases if $x > 0$ and it increases if $x < 0$. Hence two solutions appear for the limit problem. These solutions are the natural continuation one from the other. This is the suitable “regularization” to be used for the “collision” in that problems, as a blow up shows in a simple way. The natural continuation of an orbit (i.e., the one allowing to recover continuity with respect to initial conditions) is just to “cross” the origin in the same direction that the orbit has. This is in contrast with the classical two-body problem, where the regularization looks like an elastic bounce.

When we consider the problem $\dot{x} = y$, $\dot{y} = -x/(r_c^2 + x^2)$ on the level $h = 0$ of $H = y^2/2 + 0.5 \ln(r_c^2 + x^2)$ with r_c small, no relevant differences with the previous problem appear unless $|x|$ is small (of the order Kr_c , K finite). The effect of r_c is to bound y (now $|y| = \sqrt{\ln r_c^{-2}}$ at $x = 0$ instead of ∞) and “to match” the two previous solutions in the regions $x > 0$ and $x < 0$. As the time interval to go from $x = 0$ to $|x| = Kr_c$ for any finite K goes to zero with r_c in both problems, the limit period is $2\sqrt{2\pi}$ (always on the level $h = 0$; the scaling e^h is required for other energies, see Sect. 5).

Now we are interested in the normal variational equations (as presented in (31)) in the limit case $h \rightarrow \infty$. In an equivalent way we can reformulate the second of (31), rewritten as $\ddot{\xi} + \beta(r_c^2 + x^2)^{-1}\xi = 0$ with $r_c \rightarrow 0$ and x being

a solution of the first in (31), rewritten as $\ddot{x} + x/(r_c^2 + x^2) = 0$ on $h = 0$. As we are interested in values of β for which the trace of the monodromy matrix is 2 (see Sect. 5.1, Fig. 14 and related discussion), we should have a periodic solution of the normal variational equations. The n -th value of β , β_n , should correspond to a periodic solution having n full oscillations in one period, i.e., $2n$ zeros exactly. Due to symmetry properties we can select one of the zeros at $x = 0$, $y = y_{\max}$ (and, by symmetry, another at $x = 0$, $y = y_{\min}$). Hence, we are looking for a solution that vanishes at the extreme values of y and having exactly $n - 1$ zeros between them when $x > 0$. The remaining $n - 1$ zeros occur for $x < 0$.

In the limit, when $r_c \rightarrow 0$, we have the linear equation $\ddot{\xi} + \beta x^{-2}\xi = 0$ where t , x can be expressed as a function of $y = \dot{x}$ as above. Thus, using y as independent variable, we have ($' \equiv d/dy$) $\xi'' + y\xi' + \beta\xi = 0$. Let $\xi = e^{-y^2/2}g(y)$. Then the equation for g reads $g'' - yg' + (\beta - 1)g = 0$. The solutions of this equation grow slower than $e^{y^2/2}$ for $|y| \rightarrow \infty$ only if $\beta - 1 = m$ is an integer. Then we obtain $g(y) = He_m(y)$, the Hermite polynomials (see Abramowitz & Stegun 1972). They can be computed from $He_0(y) = 0$, $He_1(y) = y$, $He_{m+1}(y) = yHe_m(y) - mHe_{m-1}(y)$ for $m \geq 1$. As we want $n - 1$ real zeros of ξ , one finally has $\beta = n$.

References

- Abramowitz M., Stegun I., 1972, Handbook of Mathematical Functions. Dover
- Binney J., Spergel D., 1982, ApJ 252, 308
- Binney J., Spergel D., 1984, MNRAS 206, 159
- Binney J., Tremaine S., 1987, Galactic Dynamics. Princeton U.P. (BT87)
- Broer H., Levi M., 1995, Arch. Rat. Mech. An. 131, 225
- Broer H., Simó C., 1998, preprint, available at <http://www.maia.ub.es/dsg> (to appear in J. Diff. Eq.)
- Carpintero D., Aguilar L., 1998, MNRAS 298, 1
- Chirikov B., 1979, Phys. Rep. 52, 263
- Cincotta P., 1993, Ph.D. Thesis, La Plata University
- Cincotta P., Núñez J., Muzzio J., 1996, ApJ 456, 274
- Cincotta P., Simó C., 1999, Cel. Mech. Dyn. Astr. 73, 195
- Cincotta P., Simó C., 2000, in The Chaotic Universe, Advanced Ser. in Astroph. Cosmology, Vol. 10, Gurzadyan V., Ruffini R. (eds.). World Scientific, p. 247
- Cincotta P., Núñez J., Simó C., 2000 (in preparation)
- Contopoulos G., Seimenis J., 1990, A&A 227, 49
- Contopoulos G., Voglis N., 1996, Cel. Mech. Dyn. Astr. 64, 1
- Contopoulos G., Voglis N., 1997, A&A 317, 73
- Dehnen W., 1993, MNRAS 256, 250
- Dejonghe H., de Zeeuw T., 1988, ApJ 333, 90
- de Zeeuw T., Pfenniger D., 1988, MNRAS 235, 649
- Eddington A., 1915, MNRAS 76, 37
- Garfinkel B., 1966, AJ 71, 657
- Giorgilli A., Lazutkin V., Simó C., 1997, Reg. Chaot. Dynam. 2, 47
- Gómez G., Llibre J., Martínez R., Simó C., 1987, ESA Technical Report (to be reprinted by World Scientific, 2000), p. 270

- Hairer E., Nørsett S., Wanner G., 1987, Solving Ordinary Differential Equations I: Nonstiff Problems. Springer-Verlag
- Hénon M., Heiles C., 1964, AJ 69, 73
- Laskar J., 1990, Icarus 88, 266
- Laskar J., 1993, Phys. D 67, 257
- Laskar J., 1999, in NATO-ASI Hamiltonian Systems with Three or More Degrees of Freedom, Simó C. (ed.). Kluwer, p. 134
- Lees J., Schwarzschild M., 1992, ApJ 384, 491
- Lynden-Bell D., 1967, MNRAS 136, 101
- McGill C., Binney J., 1990, MNRAS 244, 634
- Merritt D., Friedman T., 1996, ApJ 460, 136
- Merritt D., Valluri M., 1996, ApJ 471, 82
- Miralda-Escudé J., Schwarzschild, M., 1989, ApJ 339, 752 (MS89)
- Papaphilippou Y., Laskar J., 1996, A&A 307, 427 (PL96)
- Papaphilippou Y., Laskar J., 1998, A&A 329, 451
- Patsis P., Efthymiopoulos C., Contopoulos G., Voglis N., 1997, A&A 326, 493
- Petrou M., 1983a, MNRAS 202, 1195
- Petrou M., 1983b, MNRAS 202, 1209
- Prince P., Dormand J., 1981, J. Comp. Appl. Math. 35, 67
- Reichl L., 1992, The Transition to Chaos. Springer-Verlag
- Saslaw W., 1985, Gravitational Physics of Stellar and Galactic Systems. Cambridge U.P.
- Simó C., Gómez G., Jorba A., Masdemont J., 1995, in NATO-ASI From Newton to Chaos: Modern techniques for Understanding and Coping with Chaos in N-Body Dynamical Systems, A. Roy (ed.). Plenum, p. 343
- Stiefel E., Scheifele G., 1971, Linear and Regular Celestial Mechanics. Springer-Verlag
- Udry S., Pfenniger D., 1988, A&A 198, 135
- Valluri M., Merritt D., 1998, ApJ 506, 686
- Wachlin F., Ferraz-Mello S., 1998, MNRAS 298, 22
- Whittaker E., 1917, Analytical Dynamics. Cambridge U.P.
- Wozniak H., Pfenniger D., 1999, Cel. Mech. Dyn. Astr. 73, 149